

Perturbation theory, irrep truncations, and state preparation methods for quantum simulations of $SU(3)$ lattice gauge theory

Praveen Balaji, Cianán Conefrey-Shinozaki, Patrick Draper*, Jason K. Elhaderi, Drishti Gupta, Luis Hidalgo, and Andrew Lytle

Department of Physics, University of Illinois, Urbana, IL 61801

October 7, 2025

Abstract

We study methods for efficient preparation of approximate ground states of $SU(3)$ lattice gauge theory on quantum hardware. Working in a variant of the electric basis, we introduce a refinement of the irrep truncation based on the energy density of site singlets, which provides a finer gradation of simulation complexity. Using strong-coupling perturbation theory as a guide, we develop simple ansatz circuits for ground state preparation and test them via classical simulation on small lattices, including the 2×2 plaquette lattice in $d = 2$ and the cube in $d = 3$. We contrast state fidelities and resource requirements of variational methods against adiabatic state preparation and introduce a method that hybridizes the two approaches. Finally, we report on the public release of `ymcirc`—a package of tools for building $SU(3)$ circuits and processing measurements—and `pyclebsch`, a package for efficiently computing $SU(N)$ Clebsch-Gordan coefficients.

Contents

1	Introduction	2
2	A softer irrep truncation	4
2.1	Review of the reduced electric basis	4
2.2	Site-singlet truncations	6
2.3	CGC improvements	8

*pdraper@illinois.edu

3	Ground state preparation	12
3.1	Strong-coupling perturbation theory	12
3.2	Variational ansätze	14
3.3	Results	19
3.3.1	2-plaquette Chain Lattice	19
3.3.2	Cube	21
3.3.3	Hybrid state preparation	23
3.3.4	2×2 plaquettes	24
3.3.5	5-plaquette chain	25
3.3.6	Resource costs	25
4	Simulation code: <code>ymcirc</code>	27
4.1	Available functionality	27
4.2	Development roadmap	28
5	Conclusion and Future Directions	29
A	Exact Diagonalization	36
B	Strong-Coupling Perturbation Theory Lowest Order Energy	37
C	Permutation symmetries in direct-sum decompositions	38

1 Introduction

A sufficiently advanced quantum computer could function as a unique and valuable tool for simulating quantum field theories (QFTs), providing access to nonperturbative phenomena in real time [1–4]. In particular, quantum simulations of lattice quantum chromodynamics (QCD) may be used to study parton distribution functions [5, 6], hadronization [7, 8], and classically inaccessible parts of the QCD phase diagram [9, 10], all of which are directly relevant for natural and laboratory phenomena. Schematically, these future quantum simulations will require encoding a truncation of the target Hilbert space onto the quantum computer, preparing an initial quantum state, time-evolving the quantum state according to an approximation of a target Hamiltonian, and measuring observables. Much effort has gone into developing this framework over the last decade, particularly focused on encoding and time evolution.

Several approaches have been taken to encode and time-evolve lattice gauge theories (LGTs) on digital quantum hardware. The most common starting point is the Kogut-

Susskind (KS) Hamiltonian [11, 12]. Approaches differ, in part, in how bosonic gauge link degrees of freedom are truncated and encoded while addressing the Gauss law; a non-exhaustive list includes: working with eigenstates of the electric Hamiltonian (the electric basis), labeled by irreducible representations of a continuous gauge group [13–25]; working with eigenstates of the magnetic Hamiltonian (the magnetic basis), labeled by group elements of a discrete gauge (sub)group [26–29]; and working with a hybrid of both bases [30–34].

Although observables can be calculated after time evolution on any state, a large class of interesting objects – namely correlation functions in the ground state – require the addressing the state preparation problem. Thus, quantum algorithms that prepare ground states of LGTs are necessary. A full framework for simulating QFTs (and in particular calculating scattering amplitudes in ϕ^4 theory) was developed in [35]. There, state preparation was possible because the ground state of the free theory was known and directly preparable. Then, the ground state of the interacting theory was built with adiabatic state preparation (ASP), where the free-theory ground state is evolved with a “time-dependent” Hamiltonian whose couplings are slowly turned on over time. In the case of $SU(N)$ LGT, a similar technique can be used; for example, the ground state at strong (weak) coupling is essentially the electric (magnetic) vacuum, and in principle the ground state at weaker (stronger) coupling can be prepared adiabatically from these starting points.

However, accurate ASP may require quantum circuits that are too deep for noisy intermediate-scale quantum (NISQ) computers. An alternative approach, the variational quantum eigen-solver (VQE) [36, 37], was developed as a hybrid classical-quantum algorithm that can iteratively construct a reasonable ground state with a relatively shallower circuit. The algorithm takes a reference state (which for $SU(N)$ LGT can be, for example, the electric vacuum) that is evolved with a parameterized quantum circuit, called the ansatz. The energy of the output state is then measured, and a classical optimizer tunes the ansatz parameters; the process is iterated until convergence. VQE has been used to probe a diverse range of phenomena in LGTs [38–43], including $SU(3)$ LGT [44]. It has also seen an assortment of enhancements related to optimal ansatz choice [45, 46], scalability when increasing the lattice volume [47–50], and adjustments to the ansatz based on the lattice volume [51].

With an eye towards the future goal of simulating of lattice QCD, in this work we explore methods for preparing ground states of $SU(3)$ LGT in two and three spatial dimensions. We use both VQE and ASP, and we develop two hybrid state preparation methods: one where the VQE reference state at a given coupling is the output state from a VQE performed at a higher coupling, and another where ASP is initialized with VQE. We use strong-coupling perturbation theory (PT) to motivate our VQE ansätze. Although strong-coupling PT becomes unreliable at weak coupling, the target coupling for future simulations could be in a regime where PT is still a reasonable guide. We will explore this idea in some detail on small lattices and benchmark ground state energies and eigenstate fidelities against classical exact diagonalization (ED) of the KS Hamiltonian.

Throughout this work we utilize the reduced electric basis of the KS Hamiltonian, described in [15]. This basis is an elaboration of the local multiplet basis of [14, 52, 53], which leverages the gauge invariance of physical states to greatly reduce the original electric basis of [13]. Link degrees of freedom are described by $SU(3)$ irreducible representations (irreps),

and lattice sites carry degrees of freedom that describe the gauge-singlet fusion of the irreps meeting at the site. One issue we explore is how state preparation accuracy and cost are affected by a chosen irrep truncation. A simple truncation is to cut on the electric energy of links. Roughly this energy grows with irrep dimensionality, so a variant of this truncation is to cut on the number of tensor indices in the irrep. We label T_r the truncation that keeps up to all r -index tensor irreps. However, this truncation is extremely coarse, and small changes result in rapid variations in both the maximum accessible energy density and the Hilbert space dimensionality. To improve on it we introduce a bound B on the maximum allowed electric energy density at each site. This is a finer-grained truncation, and it leads to slower growth of the number of magnetic Hamiltonian matrix elements as the truncation is relaxed. Along the way, we describe improvements to the classical precomputation of the $SU(3)$ Clebsch-Gordan coefficients (CGCs), which are inputs to the classically precomputed magnetic matrix elements, over our previous implementation [15]. The new implementation “diagonalizes” repeated irreps in the direct sum decomposition into irreps of the symmetric group acting on repeated irreps in the direct product; this has the effect of reducing the number of nonzero magnetic matrix elements. We have made the code that calculates these CGCs, `pyclebsch`, a public Python package.

Finally, we report briefly on the public release of `ymcirc`, a Qiskit-based Python package of tools to build Trotterized time evolution circuits for $SU(3)$ LGT. The public version of the code supports circuit generation for the line-of-plaquettes (“d=3/2”) lattice at the T_1 and T_2 irrep truncation, and for two-dimensional lattices at the T_1 irrep truncation, all with depth optimizations detailed in [15]. For state preparation, `ymcirc` also prepares parameterized versions of these evolution circuits for use in VQE.

2 A softer irrep truncation

Below we introduce a truncation of the Hilbert space based on an energy associated with site-singlet degrees of freedom, which feature in the reduced electric basis treatment of the Kogut-Susskind theory. We begin with a review of the reduced electric basis [15], which is based on the local multiplet basis introduced to quantum simulations of gauge theories in [14, 52, 53].

2.1 Review of the reduced electric basis

We work with the pure-gauge Kogut-Susskind Hamiltonian,

$$H = \sum_{\vec{s}} \left[\frac{g^2}{2a} \sum_i E^2(\vec{s}, \vec{e}_i) + \frac{1}{g^2 a} \sum_{i < j} 2N - \square(\vec{s}, \vec{e}_i, \vec{e}_j) - \square^\dagger(\vec{s}, \vec{e}_i, \vec{e}_j) \right] \quad (1)$$

which is a suitable lattice discretization of the continuum Yang-Mills Hamiltonian. We work with cubic spatial lattices in various dimensions and set the spacing $a = 1$. $E^2 \equiv E^b E^b$ ($b = 1, \dots, N^2 - 1$) is the quadratic Casimir operator that acts on a lattice links, and

$$\square(\vec{s}, \vec{e}_i, \vec{e}_j) = \text{tr} (U(\vec{s}, \vec{e}_i) U(\vec{s} + \vec{e}_i, \vec{e}_j) U^\dagger(\vec{s} + \vec{e}_j, \vec{e}_i) U^\dagger(\vec{s}, \vec{e}_j)) \quad (2)$$

is the plaquette operator acting on four links that trace a minimal square. \vec{s} gives the coordinates of a lattice site and \vec{e}_i ($i = 1, 2, 3$) are lattice unit vectors.

One can think of the Hilbert space as built from a (projection of) a tensor product of link Hilbert spaces. Each link Hilbert space is naturally thought of as a particle on the group manifold. In this picture the particle coordinates correspond to the magnetic basis. We work instead in the eigenbasis of E^2 , where eigenstates $|(R, r)\rangle$ are labeled by an irreducible representation (irrep) R of $SU(N)$ and a basis state r of R . Since the group admits left and right actions, a total link basis state is $|(R, r_L)\rangle \otimes |(R, r_R)\rangle \equiv |(R, r_L, r_R)\rangle$, which grants the “left” and “right” half-links independent degrees of freedom. Note that the E^2 eigenvalue, E_{R_ℓ} , of a link state only depends on the irrep R . Henceforth, we will refer to this basis as the electric basis and E_{R_ℓ} as the electric energy of a link.

Gauss’ law constrains the kinds of states that may appear on the lattice. We write physical lattice basis states in the electric basis as

$$|\Lambda\rangle = \bigotimes_{\vec{s}} \sum_r \left(\prod_{\ell \in \mathcal{L}(s)} \phi(r_\ell) \right) \langle \mathbf{1}, \Gamma_s | \otimes_{\ell \in \mathcal{L}(s)} (\bar{R}_\ell, \tilde{r}_\ell) \otimes_{\ell \in \mathcal{R}(s)} (R_\ell, r_\ell) \rangle | \otimes_{\ell \in \mathcal{L}, \mathcal{R}(s)} (R_\ell, r_{\ell, \mathcal{L}, \mathcal{R}}) \rangle \quad (3)$$

where $\ell_{\mathcal{L}}(s)$ and $\ell_{\mathcal{R}}(s)$ denote all left and right half-links appearing at site \vec{s} , and $\ell_{\mathcal{L}, \mathcal{R}}(s)$ denotes all half-links meeting at site \vec{s} . \bar{R} is a complex conjugate representation of R . (For real irreps, \bar{R} is equivalent to R .) \tilde{r} is a basis state of \bar{R} mapped from the basis state r of R . There are conventional phases in this map between bases. These conventions are partially fixed by requiring the Clebsch-Gordan coefficients (CGCs) to be real, leaving only sign conventions to fix. These signs can be identified via the Clebsch-Gordan coefficient (CGC) $\langle \mathbf{1} | (R, r) \otimes (\bar{R}, \tilde{r}) \rangle$, and $\phi(r) = \pm 1$ appearing in (3) is defined as the sign of this CGC. (We use $\mathbf{1}$ to denote the trivial representation.)

The CGC $\langle \mathbf{1}, \Gamma_s | \otimes_{\ell \in \mathcal{L}(s)} (\bar{R}_\ell, \tilde{r}_\ell) \otimes_{\ell \in \mathcal{R}(s)} (R_\ell, r_\ell) \rangle$ appearing in (3) ensures each site forms a singlet in the electric basis, thus respecting Gauss’ law. The particular singlet is determined by both the irreps meeting at the site and a multiplicity index Γ . The multiplicity index is essential because generically the group admits many invariant tensors of a given rank. For example, there are three unique singlets in $6 \otimes \bar{6} \otimes 6 \otimes \bar{6}$, and two in $8 \otimes 8 \otimes 8$. Note that all irrep basis states are summed over: therefore to specify lattice basis states $|\Lambda\rangle$, it is sufficient to assign irreps to each link, multiplicity indices to each site, and an F -order to the singlet CGCs. (The F -order specifies the order of irreps in the tensor product, a nuisance which is described further below.) This specification of basis states is called the reduced electric basis. It relaxes the costly problem of assigning singlet-admitting irreps on each link along with a consistent multiplicity index, but it leaves room for irreps that fail to admit singlets and multiplicity indices higher than those allowed by the irreps meeting at a site. Thus the total Hilbert space reflects a balance between locality and gauge-invariance.

In any electric basis, the difficult part of the Hamiltonian is the magnetic term. We write the plaquette operator in the fundamental representation f , with basis states σ . The links and sites of the plaquette are assigned irreps and multiplicity indices R_{ℓ_k} and Γ_{s_k} , respectively, for $k = 1, 2, 3, 4$. The external links, or “control” links [14] of the plaquette, meeting the plaquette at site s_k , have irreps denoted \vec{C}_{s_k} . Then the plaquette operator matrix elements can be classically and efficiently pre-computed in the reduced electric basis

from the formula

$$\langle \Lambda_n | \square | \Lambda_m \rangle = \left(\prod_{k=1}^4 \sqrt{\frac{\dim(R_{\ell_k}^m)}{\dim(R_{\ell_k}^n)}} \right) \left\{ \begin{array}{c} \bar{R}_{\ell_4}^m \quad \Gamma_{s_1}^m \quad \bar{R}_{\ell_1}^m \\ f \quad \vec{C}_{s_1} \quad \bar{f} \\ \bar{R}_{\ell_4}^n \quad \Gamma_{s_1}^n \quad \bar{R}_{\ell_1}^n \end{array} \right\} \left\{ \begin{array}{c} R_{\ell_1}^m \quad \Gamma_{s_2}^m \quad \bar{R}_{\ell_2}^m \\ f \quad \vec{C}_{s_2} \quad \bar{f} \\ R_{\ell_1}^n \quad \Gamma_{s_2}^n \quad \bar{R}_{\ell_2}^n \end{array} \right\} \\ \times \left\{ \begin{array}{c} R_{\ell_2}^m \quad \Gamma_{s_3}^m \quad \bar{R}_{\ell_3}^m \\ f \quad \vec{C}_{s_3} \quad \bar{f} \\ R_{\ell_2}^n \quad \Gamma_{s_3}^n \quad \bar{R}_{\ell_3}^n \end{array} \right\} \left\{ \begin{array}{c} \bar{R}_{\ell_3}^m \quad \Gamma_{s_4}^m \quad R_{\ell_4}^m \\ f \quad \vec{C}_{s_4} \quad \bar{f} \\ \bar{R}_{\ell_3}^n \quad \Gamma_{s_4}^n \quad R_{\ell_4}^n \end{array} \right\} \quad (4)$$

where

$$\left\{ \begin{array}{c} R \quad G \quad S \\ f \quad \vec{C} \quad \bar{f} \\ R' \quad G' \quad S' \end{array} \right\} = \sum_{\sigma=1}^{\dim(f)} \sum_{r=1}^{\dim(R)} \sum_{r'=1}^{\dim(R')} \sum_{s=1}^{\dim(S)} \sum_{s'=1}^{\dim(S')} \sum_{\vec{c} \in \vec{C}} \phi(\sigma) \\ \times \langle R', r' | (R, r) \otimes (f, \sigma) \rangle \langle S', s' | (S, s) \otimes (\bar{f}, \tilde{\sigma}) \rangle \\ \times \langle \mathbf{1}, G | (R, r) \otimes (S, s) \otimes (\vec{C}, \vec{c}) \rangle_F \\ \times \langle \mathbf{1}, G' | (R', r') \otimes (S', s') \otimes (\vec{C}, \vec{c}) \rangle_F \quad (5)$$

are site factors, and the formula assumes a CGC phase convention such that

$$\langle (A, a) \otimes (f, \sigma) | (B, b) \rangle = \phi(a) \phi(\sigma) \phi(b) \langle (\bar{A}, \tilde{a}) \otimes (\bar{f}, \tilde{\sigma}) | (\bar{B}, \tilde{b}) \rangle. \quad (6)$$

The subscript F found on the singlet CGCs reminds us that each irrep shown (R, S, \vec{C}) must be associated with a specific link on the lattice to create well-defined wavefunctions $|\Lambda\rangle$. An F -order is a conventional ordering of the links that meet at a site; it can be used to unambiguously associate each singlet CGC irrep to a lattice link. Thus, the order of the irreps in the CGC are understood to follow that of the links in the F -order.

We have described all the tools necessary, in principle, to carry out $SU(3)$ lattice simulations. However, the lattice volume and the Hilbert spaces of each link are infinite. We must impose boundaries on the lattice as well as a truncation of the link Hilbert space. The former can be done with open or periodic boundary conditions. The latter can be done in a few ways. A common approach is to cap the underlying quantum numbers of $SU(3)$ irreps, $R = (p, q)$. This places an upper bound on the electric energy of any link. Each irrep corresponds to a $p + q$ -index tensor, so a qualitatively similar truncation is to cut on the value of $p + q$. We denote this truncation by T_r , where r is the maximum value of $p + q$. For example, T_1 includes the trivial, fundamental, and antifundamental representations, and T_2 includes up to the two-index tensors.

2.2 Site-singlet truncations

The presence of site singlet degrees of freedom invites an elaboration on the electric link energy truncation. We define the electric energy associated with site \vec{s} as $\sum_{\ell(s)} E_{R_\ell}$, and we define a new truncation by placing an upper bound B on this quantity. B serves as a cutoff on the local electric energy density. B effectively truncates the link irreps, but it also truncates the possible singlets that appear at a site. This truncation scheme can greatly

reduce simulation costs, and in some cases we will see that it does so without significantly sacrificing simulation accuracy. It also allows for a finer gradation in the truncation: The jump in the number of accessible states as T_i increases is in general much greater than the increase in the number of states as B increases.

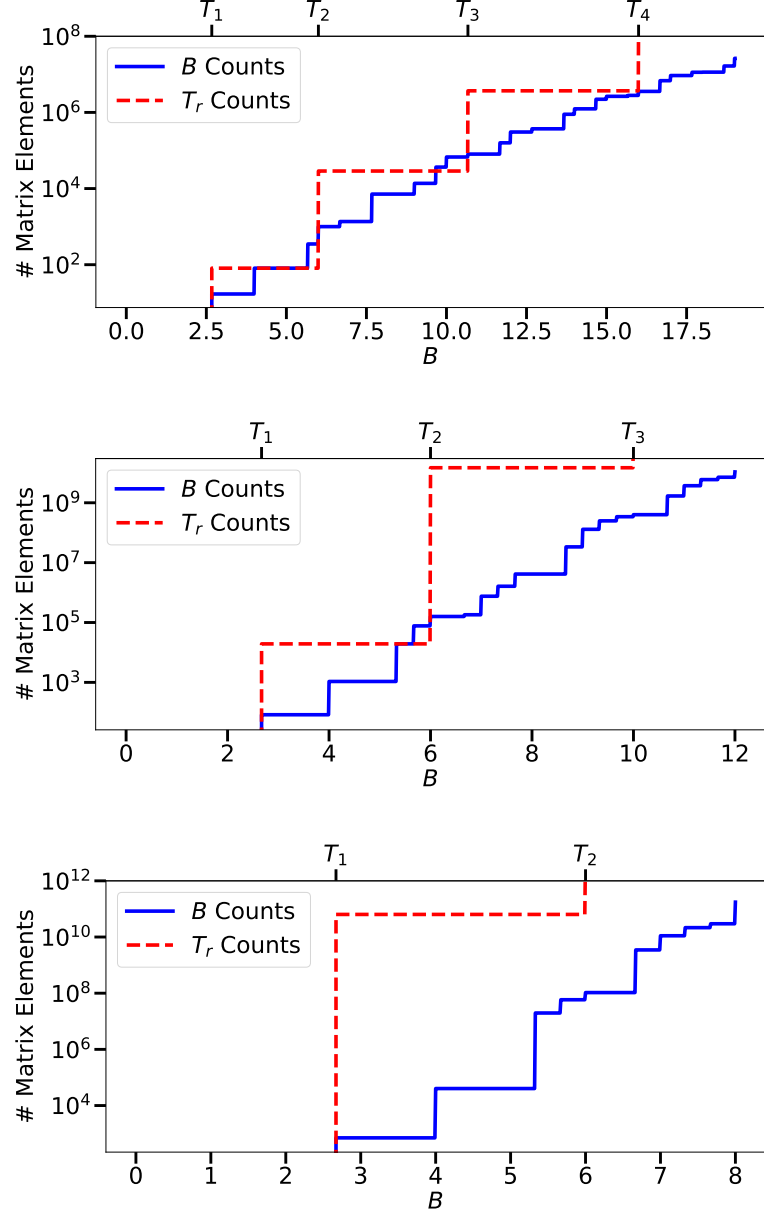


Figure 1: A comparison of \square matrix element counts in the B truncation scheme versus the T_r truncation for: $d = 3/2$ (Top), $d = 2$ (Middle), $d = 3$ (Bottom). Points marking a specific T_r indicate that B has unlocked all r -index tensor irreps. Intervals where B counts are greater than T_r counts are those where B has unlocked some but not all $r + 1$ -index tensor irreps.

In Fig. 1 we compare \square matrix element counts in both Hilbert space truncation schemes for lattices of different dimensionalities. The B truncations allow us to access irreps found in

T_r with orders-of-magnitude fewer matrix elements. In particular, by counting the number of gauge-invariant plaquette states, we estimate the T_2 truncation in $d = 3$ to involve $\gtrsim 10^{20}$ matrix elements. However, with the B truncation, *some* states involving *all* two-index tensor irreps can be accessed at $B > 6$ with $\sim 10^8$ matrix elements.

We provide tables for the singlets that are unlocked at several values of B at different spatial dimensionalities. Tables 1, 2, and 3 show the singlets accessed in the top, middle, and bottom panels of Fig. 1, respectively. $d = 3/2$ singlets in Tab. 1 are available at the same B value in $d = 2$ and $d = 3$ by tensoring the appropriate number of 1's. Likewise, $d = 2$ singlets in Tab. 2 are available at the same B value in $d = 3$ by tensoring two additional 1's. If we focus on $d = 2$, then at $B = 16/3$, the B irrep truncation coincides with T_1 . Meanwhile, $B = 6$ allows all two-index irreps in the truncation, but it is not equivalent to T_2 . For instance, $8 \otimes 8 \otimes 8 \otimes 8$, which would appear in T_2 , is still locked until $B = 12$, and the highest energy T_2 singlet, $6 \otimes 6 \otimes \bar{6} \otimes \bar{6}$, would not appear until $B = 40/3$.

Conceptually, the B truncation should be regarded as a cutoff in the sense of effective field theory, since (normalized to the number of links per vertex) it controls local energy densities, defined as an average at the lattice scale. Defining the energy density by an average over multiple sites might also be of use. The truncation needed for a given large-lattice simulation to accurately compute certain continuum observables is an important question we do not address here; however, we will investigate convergence properties of ground state energies with B at different g in various small lattices.

2.3 CGC improvements

Pre-computing the plaquette matrix elements rely on efficient computation of $SU(3)$ CGCs. Our algorithm, described in [15], is based on the algorithm of [54]. We have extended it as described in this subsection based on the algorithms of [55] (adapted from [56]) as well as [57]. This improvement results in a further reduction in the number of nonzero matrix elements as the spatial dimension and B cutoff are increased.

Our strategy for improving the CGC calculation is based on the observation that even after fixing various phase conventions, CGCs are not necessarily uniquely fixed. Of particular interest is when the same $SU(N)$ irrep appears multiple times in a direct product. More precisely, let R be an $SU(N)$ irrep, and consider the direct-sum decomposition $R^{\otimes n} = \bigoplus_i r_i$, where each r_i is also an $SU(N)$ irrep. Then a basis can be chosen so that each r_i transforms in an irrep λ of the symmetric group S_n . The CGCs of the basis states of r_i can then be symmetrized with (Hermitian) Young symmetrizers [57], and they will manifestly display the symmetries of the S_n irreps λ . This procedure is described in greater detail in appendix C.

We have implemented this “diagonalization of irreps of permutations” in our CGC code, and in Fig. 2 we compare the number of \square matrix elements found before and after CGC symmetrization for different B . We see that the symmetrized CGCs begin to reduce the matrix element counts when higher multiplicity indices begin to appear.

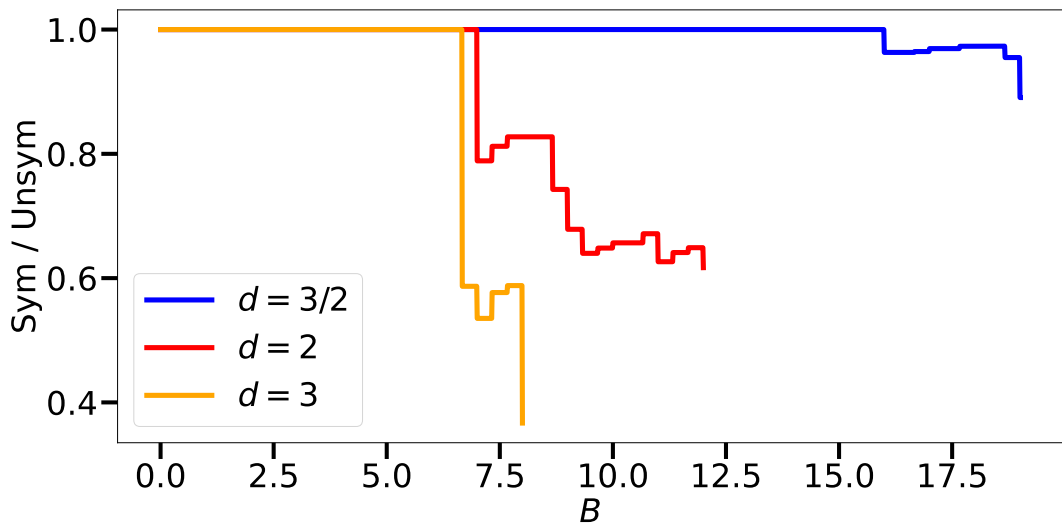


Figure 2: The reduction in \square matrix element counts using symmetrized CGCs (“Sym”) versus unsymmetrized CGCs (“Unsym”). Each curve shows the ratio $\frac{\text{Sym}}{\text{Unsym}}$ for different site-singlet energy cutoffs (B) in d dimensions. Sym counts are never higher than Unsym counts, suggesting that symmetrized CGCs are more efficient for both matrix element calculations and quantum simulations.

B	New Singlets	Multiplicity	B	New Singlets	Multiplicity
0	$1 \otimes 1 \otimes 1$	1	44/3	$3 \otimes \bar{15} \otimes 27 + \text{c.c.}$	1
8/3	$1 \otimes 3 \otimes \bar{3}$	1		$6 \otimes 8 \otimes \bar{24} + \text{c.c.}$	1
4	$3 \otimes 3 \otimes 3 + \text{c.c.}$	1		$6 \otimes \bar{6} \otimes 27$	1
17/3	$3 \otimes \bar{3} \otimes 8$	1	15	$8 \otimes 10 \otimes \bar{10}$	1
6	$1 \otimes 8 \otimes 8$	1		$3 \otimes 15 \otimes \bar{24} + \text{c.c.}$	1
	$3 \otimes 3 \otimes \bar{6} + \text{c.c.}$	1	47/3	$3 \otimes \bar{10} \otimes 24 + \text{c.c.}$	1
20/3	$1 \otimes 6 \otimes \bar{6}$	1	16	$1 \otimes 27 \otimes 27$	1
23/3	$3 \otimes 6 \otimes 8 + \text{c.c.}$	1		$15 \otimes 15 \otimes 15 + \text{c.c.}$	2
9	$8 \otimes 8 \otimes 8$	2		$6 \otimes 6 \otimes \bar{15}' + \text{c.c.}$	1
29/3	$6 \otimes \bar{6} \otimes 8$	1	50/3	$10 \otimes 15 \otimes \bar{15} + \text{c.c.}$	1
	$3 \otimes 8 \otimes \bar{15} + \text{c.c.}$	1		$6 \otimes 15 \otimes 27 + \text{c.c.}$	1
10	$6 \otimes 6 \otimes 6 + \text{c.c.}$	1		$8 \otimes 15 \otimes 24 + \text{c.c.}$	1
	$3 \otimes \bar{6} \otimes 15 + \text{c.c.}$	1		$1 \otimes 24 \otimes \bar{24}$	1
32/3	$1 \otimes 15 \otimes \bar{15}$	1		$3 \otimes 10 \otimes \bar{15}' + \text{c.c.}$	1
	$3 \otimes 6 \otimes \bar{10} + \text{c.c.}$	1	17	$8 \otimes 10 \otimes 27 + \text{c.c.}$	1
35/3	$6 \otimes 8 \otimes 15 + \text{c.c.}$	1		$6 \otimes \bar{15} \otimes 24 + \text{c.c.}$	1
12	$1 \otimes 10 \otimes \bar{10}$	1	53/3	$3 \otimes 24 \otimes 27 + \text{c.c.}$	1
	$8 \otimes 8 \otimes 10 + \text{c.c.}$	1		$6 \otimes 10 \otimes \bar{24} + \text{c.c.}$	1
	$3 \otimes 15 \otimes 15 + \text{c.c.}$	1		$8 \otimes 15 \otimes \bar{15}' + \text{c.c.}$	1
	$6 \otimes 6 \otimes \bar{15} + \text{c.c.}$	1	18	$10 \otimes 10 \otimes 10$	1
38/3	$3 \otimes 10 \otimes \bar{15} + \text{c.c.}$	1	56/3	$1 \otimes 15' \otimes \bar{15}'$	1
41/3	$8 \otimes 15 \otimes \bar{15}$	2		$15 \otimes \bar{15} \otimes 27$	2
14	$6 \otimes \bar{15} \otimes \bar{15} + \text{c.c.}$	1	19	$8 \otimes 27 \otimes 27$	2
	$8 \otimes 8 \otimes 27$	1		$3 \otimes 15' \otimes \bar{24} + \text{c.c.}$	1
44/3	$6 \otimes 10 \otimes 15 + \text{c.c.}$	1		$15 \otimes 15 \otimes \bar{24} + \text{c.c.}$	2
	$6 \otimes \bar{10} \otimes 15 + \text{c.c.}$	1			

Table 1: Singlets unlocked at several $d = 3/2$ B truncations, corresponding to those shown in the top panel of Fig. 1.

B	New Singlets	Multiplicity
16/3	$3 \otimes 3 \otimes \bar{3} \otimes \bar{3}$	2
7	$3 \otimes 3 \otimes 3 \otimes 8 + \text{c.c.}$	2
22/3	$3 \otimes \bar{3} \otimes \bar{3} \otimes \bar{6} + \text{c.c.}$	1
26/3	$3 \otimes \bar{3} \otimes 8 \otimes 8$	3
9	$3 \otimes 3 \otimes \bar{6} \otimes 8 + \text{c.c.}$	2
28/3	$3 \otimes 3 \otimes 6 \otimes 6 + \text{c.c.}$ $3 \otimes \bar{3} \otimes 6 \otimes \bar{6}$ $3 \otimes \bar{3} \otimes \bar{3} \otimes 15 + \text{c.c.}$	1 2 1
10	$3 \otimes 3 \otimes 3 \otimes \bar{10} + \text{c.c.}$	1
32/3	$3 \otimes 6 \otimes 8 \otimes 8 + \text{c.c.}$	3
11	$3 \otimes \bar{6} \otimes \bar{6} \otimes 8 + \text{c.c.}$ $3 \otimes 3 \otimes 8 \otimes 15 + \text{c.c.}$	2 2
34/3	$3 \otimes 6 \otimes 6 \otimes \bar{6} + \text{c.c.}$ $3 \otimes \bar{3} \otimes 6 \otimes 15 + \text{c.c.}$ $\bar{3} \otimes \bar{3} \otimes \bar{6} \otimes 15 + \text{c.c.}$	1 1 2
35/3	$3 \otimes \bar{3} \otimes 8 \otimes 10 + \text{c.c.}$	1
12	$8 \otimes 8 \otimes 8 \otimes 8$ $3 \otimes 3 \otimes \bar{6} \otimes 10 + \text{c.c.}$	8 1

Table 2: Singlets unlocked at several $d = 2$ B truncations, corresponding to those shown in the middle panel of Fig. 1.

B	New Singlets	Multiplicity
20/3	$1 \otimes 3 \otimes 3 \otimes 3 \otimes 3 \otimes \bar{3} + \text{c.c.}$	3
8	$3 \otimes 3 \otimes 3 \otimes 3 \otimes 3 \otimes 3 + \text{c.c.}$ $3 \otimes 3 \otimes 3 \otimes \bar{3} \otimes \bar{3} \otimes \bar{3}$	5 6

Table 3: Singlets unlocked at several $d = 3$ B truncations, corresponding to those shown in the bottom panel of Fig. 1.

3 Ground state preparation

Ground state preparation is a vital first step in exploring the dynamics of physically reasonable excited states. The goal, of course, is to leverage quantum computation beyond feasible classical algorithms.

However, in the near term quantum simulations will be limited to small lattice systems. In these cases the ground state can also be obtained by classical exact diagonalization methods, as reviewed in Appendix A. This provides a valuable benchmark for the performance of different quantum algorithms and truncation methods.

We will use perturbation theory as a guide in developing efficient quantum circuits for approximate ground state preparation. Since we are working in a variant of the electric basis, the relevant perturbative expansion is the strong-coupling expansion in small $\frac{1}{g}$, which we now review.

3.1 Strong-coupling perturbation theory

The KS Hamiltonian in Eqn. 1 can be rewritten it as $\hat{H} = \hat{H}_0 + \lambda \hat{V}$ where

$$\hat{H}_0 = \frac{g^2}{2a^{d-2}} \sum_{\text{links}} \hat{E}_\ell^2 \quad (7)$$

$$\lambda = -\frac{1}{a^{4-d} g^2} \quad (8)$$

$$\hat{V} = \sum_{\text{plaq}} \hat{\square}_p + \hat{\square}_p^\dagger \quad (9)$$

Here “links” is defined by the tuple (\vec{s}, \vec{e}_i) and “plaq” is defined by $(\vec{s}, \vec{e}_i, \vec{e}_j)$ where $i > j$. We omit for convenience the extensive, constant contribution to the magnetic Hamiltonian which makes the full Hamiltonian positive-definite. In the strong coupling regime $\hat{H} \rightarrow \hat{H}_0$, the eigenstates of which are the electric basis of the link states. The eigenvalues are proportional to the sum over the lattice of the $SU(3)$ quadratic Casimir:

$$\hat{E}^2 |p, q\rangle = \frac{p^2 + q^2 + pq + 3p + 3q}{3} |p, q\rangle \quad (10)$$

The unperturbed ground state is the product state of all links in the trivial representation, denoted $|0^{(0)}\rangle$, and with energy $E_0 = \langle 0^{(0)} | \hat{H}_0 | 0^{(0)} \rangle = 0$. As discussed in [11], excitations generated by \hat{V} are gauge-invariant excitations of a plaquette with higher dimensional irreps. Larger excitations can be built by repeated application. For finite g , the true ground state and excitations are perturbed. Since the ground state is nondegenerate, however, it is simple to find corrections to the ground state as a power series in g^{-1} [58]:

$$\begin{aligned} |0\rangle &= |0^{(0)}\rangle + \lambda |0^{(1)}\rangle + \lambda^2 |0^{(2)}\rangle + \dots \\ &= |0^{(0)}\rangle + \lambda \sum_{k \neq 0} |k_1\rangle \frac{\langle k_1 | \hat{V} | 0^{(0)} \rangle}{E_0^{(0)} - E_{k_1}^{(0)}} + \lambda^2 \sum_{k \neq 0} \frac{|k_2\rangle \langle k_2 | \hat{V} | k_1 \rangle \langle k_1 | \hat{V} | 0^{(0)} \rangle}{(E_0^{(0)} - E_{k_1}^{(0)})(E_0^{(0)} - E_{k_2}^{(0)})} + \dots \end{aligned} \quad (11)$$

where $|0^{(i)}\rangle$ compose state corrections to different orders of perturbation and the states k_1 and k_2 are lattice states in the unperturbed Hamiltonian corresponding to first-order and second-order excitations respectively. The summation excludes excitations which are identical to the unexcited ground state.

The first-order state correction can be simplified further since $\langle k_1 | \hat{V} | 0^{(0)} \rangle = 1$ for all single plaquette excitations k_1 , $E_0^{(0)} = 0$, and $E_k^{(0)} = \frac{8g^2}{3a^{d-2}}$. Using the shorthand $|k_1\rangle = |p, s\rangle$, where p is the location of the plaquette and $s = \square, \square^\dagger$ defines the two ways it can be excited, we have the first order ground state correction:

$$\lambda |0^{(1)}\rangle = \frac{3a^{2d-6}}{8g^4} \sum_{\text{plaq}} \sum_{s=\square, \square^\dagger} |p, s\rangle. \quad (12)$$

In other words, the first-order correction is a uniform superposition of an excitation at each plaquette of the lattice. Since the state-correction is order g^{-4} , the true ground state converges very quickly to the unperturbed state for $g > 1$. We may then want to consider just this first-order correction as $|0\rangle = |0^{(0)}\rangle + \lambda |0^{(1)}\rangle$. This state is not normalized, so one might include a factor of $Z^{-1} = \langle 0 | 0 \rangle$ and define a normalized state

$$|0\rangle_N = \left(1 + \frac{9N_P a^{4d-12}}{32g^8}\right)^{-\frac{1}{2}} \left(|0^{(0)}\rangle + \frac{3a^{2d-6}}{8g^4} \sum_{\text{plaq}} \sum_{s=\square, \square^\dagger} |p, s\rangle \right) \quad (13)$$

where N_P is the number of distinct plaquettes. Formally, however, this state is of mixed order in perturbation theory. The energy of this state is

$$E_0(g) = -N_P \left(1 + \frac{9N_P a^{4d-12}}{32g^8}\right)^{-1} \left(\frac{3a^{3d-10}}{4g^6} + \frac{9a^{5d-16}}{32g^{10}} \right) \quad (14)$$

This computation is carried out in Appendix B. One might wonder why the lowest order correction to the ground state energy is g^{-6} . The reason is the energy shift is given by $\Delta_0 = \lambda \langle 0^{(0)} | \hat{V} | 0^{(0)} \rangle + \lambda^2 \langle 0^{(0)} | \hat{V} | 0^{(1)} \rangle + \mathcal{O}(\lambda^3)$, and since the magnetic perturbation \hat{V} in the electric basis is zero on the diagonal, we see that the lowest order shift is proportional to $\lambda^2 E_p^{-1} \sim g^{-6}$. Observe also that the energy of the normalized corrected state is again not of fixed order in perturbation theory. Keeping only the lowest orders we have

$$E_0^{(1)}(g) = -N_P \left(\frac{3a^{3d-10}}{4g^6} + \frac{9a^{5d-16}}{32g^{10}} \right). \quad (15)$$

Normally the mixed-order g^{-10} term in Eqn. 14 for E_0 should be discarded, because the second-order state correction could introduce new corrections to order g^{-10} . However this does not happen. The g^{-10} terms from $|0^{(2)}\rangle$ are $2\lambda^3 \langle 0^{(2)} | \hat{H}_0 | 0^{(1)} \rangle$ and $2\lambda^3 \langle 0^{(2)} | \hat{V} | 0^{(0)} \rangle$. However $\hat{H}_0 |0^{(1)}\rangle + \hat{V} |0^{(0)}\rangle = 0$, so these terms cancel. Thus the first-order state correction contains the two lowest order corrections entirely, and second-order state corrections would correct to third lowest order, g^{-14} . This highlights the surprising strength of the first-order state correction as shown in Fig. 3. We also emphasize this formula for the first-order state correction holds regardless of the number of plaquettes, lattice geometry, or the truncation of irreps. Higher-order corrections will depend on all of these factors.

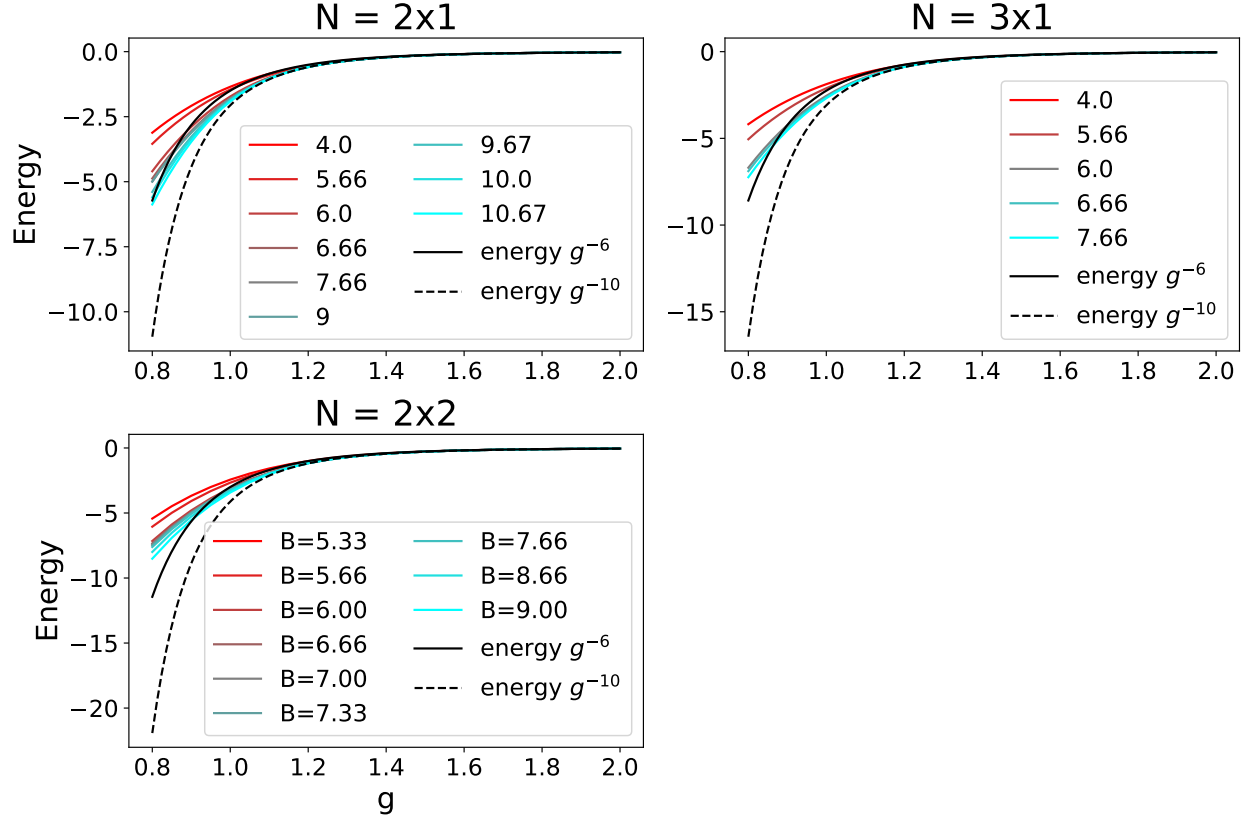


Figure 3: Comparison of strongly-coupled perturbation theory with exact diagonalization results. Note that as B increases, the number of matrix elements for \square and the number of $SU(3)$ irreps included increases as seen in Fig. 1 and in Table 1. For example, in $d = 3/2$, the 8 appears at $B = 5.67$, the 6 appears at $B = 6$ and the 15 appears at $B = 9.67$.

While we see good convergence of perturbation theory to the exact data even around $g = 1.2$, for g below unity the truncated series quickly becomes a poor approximation to the ground state. We also observe in Fig. 3 an empirical convergence of the ground state energy for fixed g as the singlet energy cutoff B is increased. The target for future quantum simulations is probably a lattice coupling around $g = 1$, so we can hope that perturbation theory is a useful qualitative guide for more precise algorithms. Next we explore some ansatze that can provide a basis for VQE methods.

3.2 Variational ansätze

In the following it will be convenient to define the KS Hamiltonian as

$$\hat{H} = g^2 \hat{H}_E + \frac{1}{g^2} \hat{H}_B. \quad (16)$$

and set $a = 1$ for the remainder of the paper. We will examine different variational ansatz circuits utilizing elements of the Trotterized time-evolution circuits developed in the `ymcirc`

package described below. These time-evolution circuits can be characterized as either evolving the electric part of the Hamiltonian or evolving the magnetic part of the Hamiltonian. We call the circuit for electric evolution circuit $E(t)$ and that for magnetic evolution $M(t)$, such that

$$E(g^2 t) = e^{-i g^2 \hat{H}_E t} \quad (17a)$$

$$M(t/g^2) = e^{-i \hat{H}_B t/g^2}. \quad (17b)$$

Our first ansatz circuit is build from successive applications of the (E)lectric and (M)agnetic circuits to the electric vacuum, replacing the time-evolution parameter t with the generalized parameters $\{\theta_i\}$ (we absorb any factors of g into the parameters). The variational algorithm then attempts to find a local minimum for the expectation value of the energy in the state space spanned by the θ_i . The successive applications of $E(\theta_i)$ and $M(\theta_j)$ in different combinations produces a family of operators, any fixed choice of which could be used as the ansatz. We focus first on the simplest combinations: (a) $E(\theta_2)M(\theta_1)$, and (b) $E(\theta_4)M(\theta_3)E(\theta_2)M(\theta_1)$. This has a flavor of the well-known Lanczos algorithm, where powers of the Hamiltonian are successively applied to an initial state [59]. However here we allow the parameters θ_i to differ significantly from their values in the Hamiltonian and also do not include “cross-terms” that would emerge like EE or MM . The inspiration for these choices lies in strong-coupling perturbation theory.

Let us first consider first-order perturbation theory. As discussed in Section 3.1 the (un-normalized) approximation to the ground state up to the first order in $1/g$ is given by

$$\begin{aligned} |0\rangle &= |0^{(0)}\rangle - \frac{1}{g^2} \sum_{k_1} \frac{\langle k_1 | \hat{H}_B | 0^{(0)} \rangle}{E_{k_1}} |k_1\rangle + \mathcal{O}(1/g^8) \\ &= |0^{(0)}\rangle + \frac{3}{8g^4} \sum_{k_1} |k_1\rangle + \mathcal{O}(1/g^8) \end{aligned} \quad (18)$$

where the $|k_1\rangle$ states refer to single-plaquette excitations of the lattice and $E_{k_1} = 8/3g^2$ (note that this value is obtained by calculating the value of H_E for all the excited links in the plaquette). Now, let us consider the parametric operator $M(\theta_1)$. In the strong-coupling limit when θ_1 is sufficiently small, we can perturbatively expand the action of M on the electric vacuum such that

$$M(\theta_1) |0^{(0)}\rangle = |0^{(0)}\rangle - i\theta_1 \hat{H}_B |0^{(0)}\rangle + \mathcal{O}(1/g^8). \quad (19)$$

Because the action of the plaquette operator (of which \hat{H}_B is made up) leads to exactly the single-plaquette excitations $|k_1\rangle$, the above equation can also be written as

$$M(\theta_1) |0^{(0)}\rangle = |0^{(0)}\rangle + i\theta_1 \sum_{k_1} |k_1\rangle + \mathcal{O}(\theta_1^2) \quad (20)$$

Therefore, the form of the strong-coupling expansion for $M(\theta_1)$ matches with perturbation theory up to the first order. However, the coefficient of the first order term in the expansion of $M(\theta_1)$ has an extra i , which cannot be reconciled with first-order perturbation theory

unless θ_1 is also imaginary. This is not allowed since $M(\theta_1)$ is unitary. To remedy the situation we introduce the operator $E(\theta_2)$ in Eqn. 20 such that

$$E(\theta_2)M(\theta_1)|0^{(0)}\rangle = |0^{(0)}\rangle + i\theta_1 e^{-8i\theta_2/3} \sum_{k_1} |k_1\rangle + \mathcal{O}(\theta_1^2). \quad (21)$$

Comparing Eqn. 18 and Eqn. 20, we find that in order to match the first order perturbative expansion,

$$\theta_1 = 3/(8g^4), \quad \theta_2 = 3\pi/16. \quad (22)$$

Notice that while θ_1 is perturbative in the strong-coupling limit, the value of θ_2 is not perturbative as $E(\theta_2)$ is introduced just to fix a relative phase.

Therefore, the parametric state $E(\theta_2)M(\theta_1)|0^{(0)}\rangle$ is expected to be a good ansatz in the strong-coupling region. For brevity, we will call this the EM ansatz. In Fig. 4, we plot the 90% and 94% energy contours in the $\{\theta_1, \theta_2\}$ parameter space, along with the parameters obtained in the minimization algorithm, for the $d = 2$ lattice with 2×2 plaquettes with couplings $g = 1.0$, $g = 1.4$, and $g = 1.8$ in the $B = 4.0$ energy truncation. For $g = 1.8$ and $g = 1.4$, the agreement of the parameters obtained by VQE and that predicted by strong-coupling perturbation theory is excellent, whereas that for $g = 1.0$ the fit deviates from PT.

To improve on the EM ansatz, we turn to second-order perturbation theory. The action of $M(\theta_1)$ on the electric vacuum up to second order in the parameter is given as

$$M(\theta_1)|0^{(0)}\rangle = |0^{(0)}\rangle + i\theta_1 \sum_{k_1} |k_1\rangle - \frac{\theta_1^2}{2} \sum_{\mathcal{E}=0}^{20/3} \sum_{\{E(k_2)=\mathcal{E}\}} \sigma(k_2) |k_2, \mathcal{E}\rangle + \mathcal{O}(\theta_1^3). \quad (23)$$

The coefficient $\sigma(k_2)$ is the matrix element denoting the amplitude of this transition, i.e., $\sigma(k_2) = \langle k_2 | \hat{H}_B^2 | 0^{(0)} \rangle$. The $|k_2, \mathcal{E}\rangle$ are the two-plaquette excitations obtained by successively applying the plaquette operators, i.e. $|k_2, \mathcal{E}\rangle = -\hat{H}_B |k_1\rangle$, and with an index given by their H_E eigenvalue \mathcal{E} . Accordingly, the sum over all the two-plaquette excitations is split over all the distinct \mathcal{E} that result from a two-plaquette excitation (see Table 4), and over all the two-plaquette excitations that have the same \mathcal{E} . Applying the $E(\theta_2)$ operator on both sides, we get

$$E(\theta_2)M(\theta_1)|0^{(0)}\rangle = |0^{(0)}\rangle + i\theta_1 e^{-8i\theta_2/3} \sum_{k_1} |k_1\rangle - \frac{\theta_1^2}{2} \sum_{\mathcal{E}=0}^{20/3} e^{-i\mathcal{E}\theta_2} \sum_{\{E(k_2)=\mathcal{E}\}} \sigma(k_2) |k_2, \mathcal{E}\rangle \quad (24)$$

Applying the EM combination one more time, we get

$$\begin{aligned} E(\theta_4)M(\theta_3)E(\theta_2)M(\theta_1)|0^{(0)}\rangle &= |0^{(0)}\rangle + ie^{-8i\theta_4/3}(\theta_1 e^{-8i\theta_2/3} + \theta_3) \sum_{k_1} |k_1\rangle \\ &\quad - \sum_{\mathcal{E}=0}^{20/3} e^{-i\mathcal{E}\theta_4} \left(\frac{\theta_1^2 e^{-i\mathcal{E}\theta_2}}{2} + \frac{\theta_3^2}{2} + \theta_1 \theta_3 e^{-8i\theta_2/3} \right) \sum_{\{E(k_2)=\mathcal{E}\}} \sigma(k_2) |k_2, \mathcal{E}\rangle. \end{aligned} \quad (25)$$

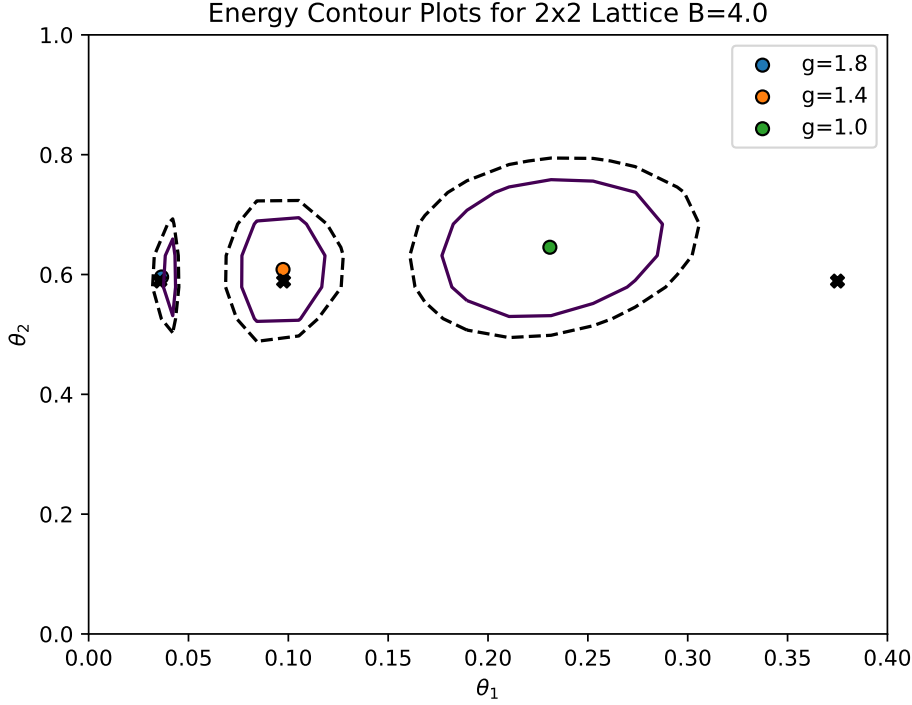


Figure 4: Energy contours for the EM ansatz states on the 2×2 plaquette lattice with periodic boundary conditions and $B = 4.0$ energy truncation. The black crosses denote the prediction of strong-coupling PT, while the colored dots denote the local minima. Solid and dashed contours denote 6% and 10% deviations from the minima, respectively.

In strong coupling PT, Eqn. 11 tells us

$$|0^{(2)}\rangle = \frac{3}{8g^8} \sum_{\mathcal{E}=8/3}^{20/3} \frac{1}{\mathcal{E}} \sum_{\{E(k_2)=\mathcal{E}\}} \sigma(k_2) |k_2, \mathcal{E}\rangle \quad (26)$$

so, up to the second order, the perturbative ground state is given by

$$|0\rangle = \left(1 - \frac{9N_P}{64g^8}\right) |0^{(0)}\rangle + \frac{3}{8g^4} \sum_{k_1} |k_1\rangle + \frac{3}{8g^8} \sum_{\mathcal{E}=8/3}^{20/3} \frac{1}{\mathcal{E}} \sum_{\{E(k_2)=\mathcal{E}\}} \sigma(k_2) |k_2, \mathcal{E}\rangle. \quad (27)$$

where N_P is the number of plaquettes in the lattice. Thus, while the expression for the perturbative expansion of the EMEM ansatz matches qualitatively with the strong-coupling expansion of the ground state, the former does not have enough free parameters to match the latter exactly: matching Eqs. 25 and 27 amounts to nine equations, corresponding to the number of sets of single and double plaquette excitations that have distinct electric energies \mathcal{E} , whereas we only have four independent parameters in the EMEM ansatz. In smaller B truncations the higher \mathcal{E} excitations may be prohibited, so EMEM is a more effective ansatz for such truncations.

The gate depth cost of the EM and EMEM ansätze scale essentially as one and two Trotter steps, respectively. We can do better, and improve on the ansatz quality, by considering circuits with more variables.

In our approach to time evolution each distinct magnetic transition is implemented sequentially, on each plaquette, by two-level unitaries known as Givens rotations \hat{G}_j where \hat{G}_j^2 is the identity. Now let us consider an ansatz again based on the time evolution circuits, but for which each magnetic Givens rotation is assigned an independent parameter. Below we refer to ansätze of this type – and restrictions to subsets of the most important two-level transitions – as “multi-Givens”.

We create an ansatz with parameters over 8 different classes of Givens rotations such as given in Table 4. The operator \hat{G}_1 jumps the electric vacuum into a single-plaquette excitation. It is like the magnetic Hamiltonian, restricted to just those matrix elements that are connected to the electric vacuum. Its effect is given (up to second order in the parameter θ_1) by

$$e^{-i\hat{G}_1\theta_1} |0^{(0)}\rangle = (1 - \theta_1^2 N_P) |0^{(0)}\rangle + i\theta_1 \sum_{k_1} |k_1\rangle - \frac{\theta_1^2}{2} \sum_{k_1, k'_1} |k_1\rangle \otimes |k'_1\rangle \quad (28)$$

where k_1 and k'_1 are single-plaquette excitations on disjoint plaquettes, i.e. plaquettes that share neither a corner nor edge. The rest of the Givens operators connect non-vacuum plaquette states, and so they only act nontrivially once the plaquette state (or more precisely, the state of the plaquette and its control links) is excited. Thus $\hat{G}_j |0^{(0)}\rangle = 0$ for $j \neq 1$. Following \hat{G}_1 their combined effect on the electric vacuum is given (again up to second order in the parameters) by:

$$\begin{aligned} \prod_{j=2}^8 e^{-i\sigma(k_j)\hat{G}_j\theta_j} e^{-i\hat{G}_1\theta_1} |0^{(0)}\rangle &= (1 - \theta_1^2 N_P) |0^{(0)}\rangle + i\theta_1 \sum_{k_1} |k_1\rangle \\ &\quad - \sum_{j=2}^8 \theta_1 \theta_j \sum_{\{E(k_2)=\mathcal{E}(j)\}} \sigma(k_2) |k_2, \mathcal{E}\rangle - \frac{\theta_1^2}{2} \sum_{k_1, k'_1} |k_1\rangle \otimes |k'_1\rangle. \end{aligned} \quad (29)$$

In order to fix the relative phases between the zeroth, first and second orders, we introduce an electric operator that adds a phase to the single plaquette excitation. Such an operator can be built by a multi-control phase gate wherein the controls are given by the active links of a single plaquette excitation. We will call this phase operator \hat{P}_1 , with associated parameter $\tilde{\theta}_1$. After applying the exponent of this operator to both sides, we obtain

$$\begin{aligned} e^{-8i\hat{P}_1\tilde{\theta}_1/3} \prod_{i=1}^8 e^{-i\sigma(k_i)\hat{G}_i\theta_i} |0^{(0)}\rangle &= (1 - \theta_1^2 N_P) |0^{(0)}\rangle + i\theta_1 e^{-8i\tilde{\theta}_1/3} \sum_{k_1} |k_1\rangle \\ &\quad - \frac{\theta_1^2}{2} e^{-16i\tilde{\theta}_1/3} \sum_{k_1, k'_1} |k_1\rangle \otimes |k'_1\rangle - \sum_{j=2}^8 \theta_1 \theta_j e^{-16i\tilde{\theta}_1\delta_{j4}/3} \sum_{\{E(k_2)=\mathcal{E}(j)\}} \sigma(k_2) |k_2, \mathcal{E}\rangle. \end{aligned} \quad (30)$$

Comparing this to second order state in Eqn. 27, we find that strong-coupling PT predicts

$$\begin{aligned}\theta_1 &= \frac{3}{8g^4} + \frac{9}{64g^8}, & \theta_2 &= -\frac{1}{4g^4}, & \theta_3 &= -\frac{3}{14g^4}, \\ \theta_4 &= \frac{3}{16g^4}, & \theta_5 &= -\frac{6}{33g^4}, & \theta_6 &= -\frac{3}{17g^4}, \\ \theta_7 &= -\frac{1}{6g^4}, & \theta_8 &= -\frac{3}{20g^4}, & \tilde{\theta}_1 &= \frac{3\pi}{16}.\end{aligned}\quad (31)$$

Notice that even though there are three equations for θ_1 when we match the zeroth, first orders, and the disjoint plaquette parts of the ansatz and perturbation theory, the solution $\theta_1 = 3/(8g^4) + 9/(64g^8)$ is consistent with all three orders.¹

The above analysis holds for general lattices in general dimensions. Moreover, selectively choosing Givens operators based on matching with perturbation theory can give a systematic way of improving the accuracy of the ansatz up to a given order in $1/g$.

We also demonstrate in later sections that selecting Givens rotations based on how “important” they are in creating the ground state can lead to significant savings in the gate depth of the state preparation circuits.

3.3 Results

It is straightforward to test state preparation algorithms in classical simulations of small lattice systems. Below we compare the variational methods described above for the 2-plaquette chain with periodic boundary conditions, the cube with open boundary conditions, and the 2×2 plaquette lattice with periodic boundary conditions. We compare the ground state energy obtained with exact diagonalization for various B truncations to the expectation value of the energy in the best-fit ansatz states. We also compute the fidelity of the ansatz states (defined by comparison to exact diagonalization) and compare with adiabatic state preparation.

3.3.1 2-plaquette Chain Lattice

We begin with the 2-plaquette chain, varying the parameters of the EM and EMEM ansätze defined in Sec. (3.2) until a (local) minima for the expectation value of the Kogut-Susskind Hamiltonian is obtained. The Broyden-Fletcher-Goldfarb-Shanno algorithm that is built into SciPy’s `minimize` method was used to reach this minima up to a specified precision. The ability of any minimization algorithm to find the global minimum depends on the values of the initialization parameters fed into the algorithm. In our particular case, it is easy to guess the values of initialization parameters that should be fed into the algorithm for larger values of the coupling constants, where we can use perturbation theory directly (see Sec. (3.2)).

¹Observe in Eqn. 27 that there are double-excitations that look like single-excitations. This follows from the fact that $1 = \langle 0^{(0)} | \square^3 | 0^{(0)} \rangle = \langle \square^\dagger 0^{(0)} | \square^2 0^{(0)} \rangle$. θ_1 includes these double-excitation terms and thus has this higher-order contribution.

Plaquette excitation	\mathcal{E}	Givens Operators
Single Plaquette Excitations		
	8/3	\hat{G}_1, \hat{P}_1
Two Plaquette Excitations		
	12/3	\hat{G}_2
	14/3	\hat{G}_3
	16/3	\hat{G}_4
	11/2	\hat{G}_5
	17/3	\hat{G}_6
	18/3	\hat{G}_7
	20/3	\hat{G}_8

Table 4: Givens operator groups. Each group \hat{G}_i denotes Givens rotations that have the same electric energy. The notation is such that \hat{G}_j for $j > 1$ refers to single-plaquette magnetic transitions that connect non-electric-vacuum states, one of which is a single-plaquette excitation. Thus the h.c. in the loop of 8 is a reminder that it can be formed either from an application of \square then \square^\dagger , or \square^\dagger then \square .

However, perturbation theory predictions fail to provide good initialization parameters at weak coupling. Therefore we use a modified variational algorithm in which estimates for initialization parameters are obtained by successively running the optimization starting from a fixed strong coupling point and adiabatically decreasing the value of the coupling constant, recursively feeding the optimal parameters obtained for g_n as the initialization parameters

for g_{n+1} until the target coupling is reached.

We compare the ground state energies obtained by the variational algorithm with those obtained by exact diagonalization in Fig. 5. We see that as the site singlet energy cutoff B is increased, the relative error between the energies of VQE with EM/EMEM ansatz and exact diagonalization energies increases, indicating that a better ansatz with more parameters is needed for higher B -cutoffs. However, EMEM improves significantly on EM, and remains good to better than 10% even down to $g = 0.8$ for $B = 9$ (which includes, for example, some singlets involving $6, \bar{6}, 8$.)

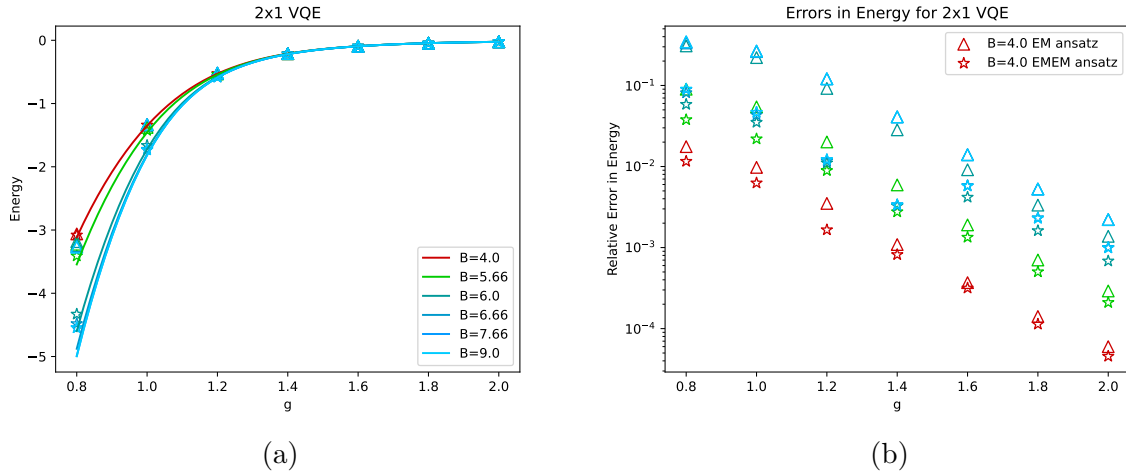


Figure 5: (a) Comparison of ground state energies obtained by VQE using the EM and EMEM ansätze to exact diagonalization for different values of energy truncation B . The solid lines depict the exact diagonalization energies, the triangles depict the energies obtained using the EM ansatz, and the stars depict the energies obtained using the EMEM ansatz. (b) Relative error in energies obtained by VQE with respect to exact diagonalization. The markers for EM and EMEM are the same as (a).

3.3.2 Cube

The modified variational optimization procedure described in Sec. (3.3.1) can be implemented on larger lattices. The three dimensional cube with open boundary conditions is relatively easy to study in the T_1 truncation (equivalent to $B = 4.0$ for this lattice) because the circuits are shallow and the qubit count is limited. In addition to the EM and EMEM ansätze used in Sec. (3.3.1), we test the “multi-Givens” ansatz described earlier. In this ansatz a restricted collection of magnetic transitions is utilized, each with a different parameter. Here our choice of this collection is motivated by strong coupling PT; in practice we perform a fit at $g = 2$ with all rotations given a free parameter, then select only those rotations for which the fit assigns a nonzero parameter. Without this cut, the CX gate count is $\sim 26,000$, but removing the relatively less important Givens rotations reduces this count to $\sim 8,000$.

In larger lattices, finding the minima of the energy function by iterating over the ansatz circuits might become a computationally expensive task. One approach is to weave together

circuits for small lattices into larger ones by successive applications of VQE [44]. Testing the weaving approach on small enough systems to simulate classically would be an interesting direction for future study.

Another approach to state preparation is the adiabatic method. In Fig. 6 we compare the energies and the relative error in energy obtained for the cube lattice by different methods of state preparation. We see that all methods work fairly well down to $g \sim 1$. At lower g , adiabatic state preparation outperforms our variational ansätze. At larger g , the quality of the adiabatic method depends on the starting point. To illustrate this, we include two adiabatic curves, corresponding to different initial values of g . Starting the adiabatic evolution from the electric vacuum in the far strong coupling regime leads to a more stable evolution than starting at $g = 2.0$, since the electric vacuum is a better approximation to the ground state in the strong coupling regime. However, starting the adiabatic evolution from a higher value in g has a tradeoff in gate counts. In the figure, ~ 300 Trotter steps were used to adiabatically evolve the electric vacuum to $g = 1.0$ from $g = 4.0$, and ~ 100 Trotter steps were used to evolve to $g = 1.0$ from $g = 2.0$. Of course, this can be improved by using a better perturbative starting point, or by a hybrid adiabatic-variational method discussed in the next subsection.

In Fig. 7 we show the state fidelity, the probability of obtaining the true ground state (defined as statevector obtained by exact diagonalization) in the prepared approximate ground state. Small-step adiabatic preparation achieves the best results at small g , and is systematically improvable by either increasing the starting value of g or improving the starting state. However, the multi-Givens ansatz, based on the most important magnetic transitions at strong coupling, achieves percent-level fidelity down to $g \sim 1.0$.

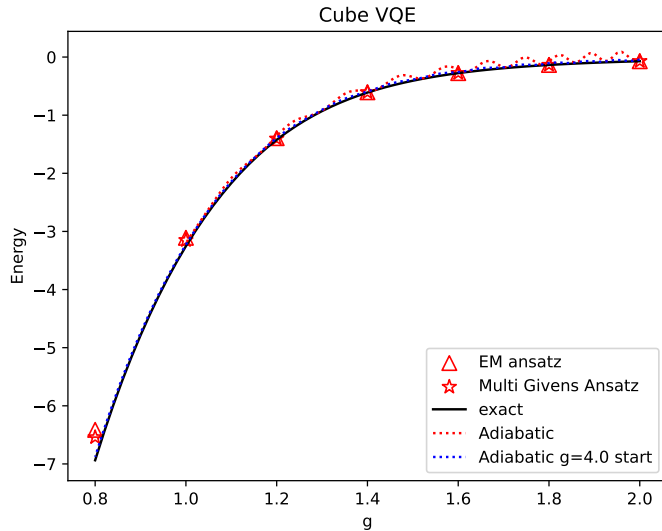


Figure 6: Comparison of cube lattice ground-state energy obtained via variational methods with the EM and multi-Givens ansätze described in the text; exact diagonalization; and adiabatic state preparation starting from $g = 4$ (blue) and $g = 2$ (red) respectively, with adiabatic step sizes of $\Delta g = 0.01$ in the $B = 4.0$ (or equivalently, the T_1) truncation.

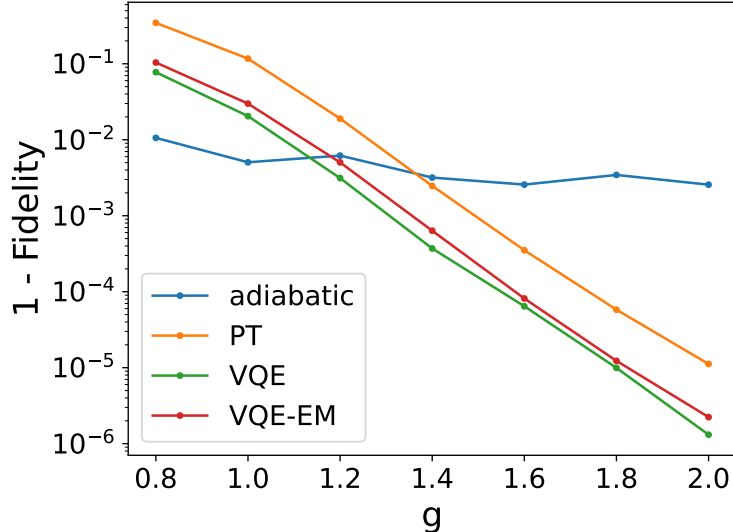


Figure 7: Fidelity of the approximate ground state prepared using the adiabatic method, the variational method with EM ansatz (“VQE-EM”), the variational method with the multi-Givens ansatz (“VQE”), and lowest order perturbation theory. Here fidelity refers to $|\langle \psi_{\text{ED}} | \psi \rangle|^2$ where ψ_{ED} is the ground state obtained via exact diagonalization. The most interesting result is that the relatively shallow multi-Givens ansatz achieves percent-level fidelity at $g \sim 1$.

3.3.3 Hybrid state preparation

We have seen that for small lattices, both variational ansätze and adiabatic methods generate accurate approximations to the ground state. The variational method has an up-front cost driven by the iterative procedure to find the parameters for the given ansatz with maximal ground state overlap. Once these parameters have been determined, the state preparation then requires only (relatively) shallow circuits, of a depth comparable to one (for EM) or two (for EMEM) steps of Trotter evolution, and significantly less for the multi-Givens ansatz. At smaller couplings we observe that the ability of the ansatz states to capture the true ground state degrades somewhat.

On the other hand, the adiabatic algorithm maintains a strong overlap with the true ground state roughly independent of the value of g (see e.g. Fig. 7). However, since the evolution begins at large g , the preparation circuit becomes deep as g is decreased. This makes state preparation inefficient, especially since the evaluation of ground state observables will generically require preparing the ground state repeatedly to build up measurement statistics.

To minimize state depth while maintaining strong ground state overlap irrespective of g , we consider a hybrid strategy that uses the optimized VQE circuit for g up to some threshold value and then “switches on” adiabatic preparation when simulating at g below that threshold.² In cases where the true ground state is known, one can compute $1 - F$ as a function of g for both methods. The adiabatic runs can now be considered part of the

²A similar strategy has previously been used in initial state preparation of scalar lattice ϕ^4 theory [60].

“up front” cost, similar to the optimization runs. The threshold can be taken to be a g near where the adiabatic and variational ansatz curves cross (see e.g. Figs. 7 and 8).

In the more interesting case when the true ground state is not known, a threshold value must be inferred in order to use the hybrid approach. One possibility is to choose a threshold motivated by strong-coupling PT and then empirically measure the sensitivity of the ASP state at lower g to small variations in the threshold.

Here we demonstrate the hybrid method using the cube lattice. Fig. 8 repeats the fidelities, this time comparing the fidelities obtained by adopting a hybrid “adiabatic-EM” approach to that obtained by the multi-Givens and adiabatic approach described in the previous section. The hybrid adiabatic state preparation is turned on around $g = 1.4$, for which the VQE preparation circuits have a $1 - F \sim 10^{-3}$. The $1 - F$ value of the hybrid adiabatic evolution is very similar to that of adiabatic evolution at $g = 0.8$, but the circuit depth for the hybrid approach is significantly lower, as the hybrid approach only needs ~ 25 Trotter steps to reach $g = 0.8$, whereas the adiabatic approach needs ~ 300 steps. Therefore, the hybrid approach affords fidelities comparable to the traditional adiabatic approach at a much lower gate cost.

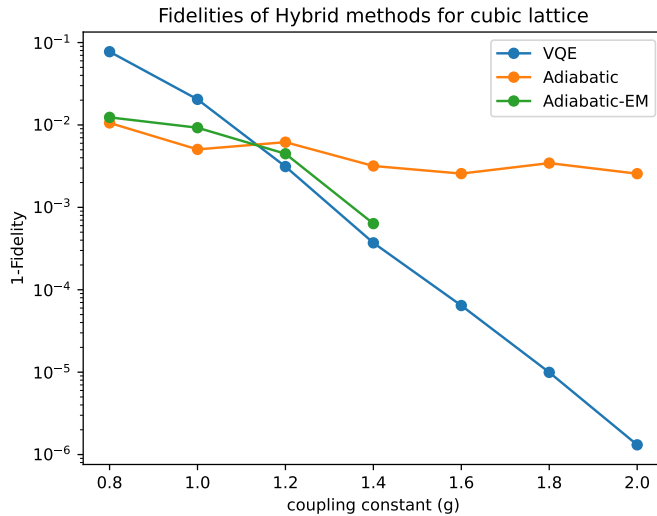


Figure 8: Fidelities for different state preparation methods on the cube. The hybrid method Adiabatic-EM first uses the optimized VQE-EM circuit from $g = 1.4$ and then use the adiabatic algorithm to compute the ground state at smaller g .

3.3.4 2×2 plaquettes

As an example in two dimensions we consider the 2×2 lattice with periodic boundary conditions. In Fig. 9a we compare the energy obtained with exact diagonalization, for different values of the B cutoff, to the variational ansatz results.

To get a sense for the makeup of the ground state, Fig. 9b shows the probabilities of finding different excited states in the variational ground state with $B = 6$. While the probability

of finding single plaquette and double plaquette excitations in the strong-coupling limit $g = 2$ is vanishingly small, the probabilities to find these excitations steadily increase as one approaches $g \sim 1$; in fact, the single plaquette excitations dominate the electric vacuum in the ground state for $g = 0.8$. However, the double-plaquette excitations are subdominant even for $g = 0.8$, explaining the surprising performance of the EMEM ansatz towards capturing the ground state for such weak couplings.

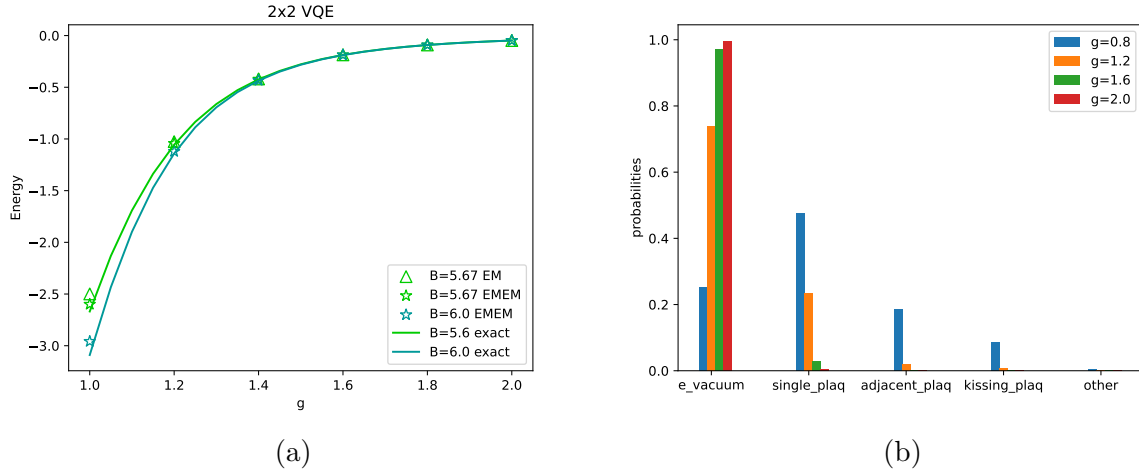


Figure 9: (a) Comparison of VQE with the EM and EMEM ansätze with the exact diagonalization of the 2×2 plaquettes for $B = 5.67$ and $B = 6.0$, and (b) Characterization of the states obtained in the $B = 6.0$ VQE state preparation using the EMEM ansatz. “e_vacuum” refers to the electric vacuum, “single_plaq” refers to single plaquette excitations, and “adjacent_plaq” and “kissing_plaq” refer to the two type of double plaquette excitations possible in the 2×2 lattice, which are the excitations that share an edge and a vertex respectively.

3.3.5 5-plaquette chain

For N -plaquette chains, with fixed classical memory resources, there is a tradeoff between the maximum N and B that may be simulated, i.e., as N increases the maximum B that can be simulated decreases. In Fig. 10 we show results for the ground state energy of the 5-plaquette chain with $B = 4$.

With a global encoding of the Hilbert space, instead of a local encoding, and a low irrep truncation, it is possible to study chains of 10+ plaquettes. These analyses, along with a more extensive comparison of global vs. local approaches, will be presented elsewhere.

3.3.6 Resource costs

We conclude this section with Table 5, sketching the approximate quantum resource costs of preparing ground states for the cube, 2×2 , and 5 plaquette lattices using the methods described above.

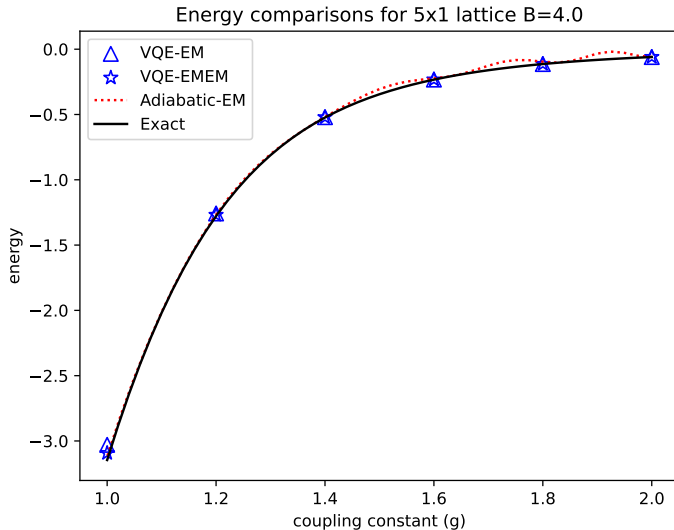


Figure 10: Comparisons of ground state energies computed with the variational EM and EMEM methods, exact diagonalization, and hybrid adiabatic state preparation, for the 5-plaquette lattice with $B = 4.0$ truncation.

The resources needed to prepare the ground state generally depend on (1) the number of qubits needed to encode the lattice, and (2) the circuit depth of one Trotter step, which directly controls the circuit depth of the VQE and adiabatic circuits. One Trotter step for the cube with open boundary conditions has a CX gate count $\sim 26,000$, which also corresponds to the gate count of the EM preparation circuits (denoted by VQE-EM) because applying the EM operator is equivalent to one Trotter step. The gate cost of one Trotter step can be reduced to about $\sim 8,000$ by choosing the Givens rotations that are “important” and individually parameterizing the rotations (this method is denoted by VQE-MTI). The EMEM preparation circuits have twice the gate count of one Trotter step. The adiabatic preparation circuits, however, are significantly deeper than the variational circuits, because they correspond to many Trotter steps. For example, the adiabatic evolution from $g = 4.0$ to $g = 1.8$ with adiabatic step size $\Delta g = 0.01$ requires 320 steps, thereby increasing the depth of the adiabatic preparation circuits by a factor of ~ 300 . Choosing a hybrid approach allows us to start from a lower value of g and increase the adiabatic step size to $\Delta g = 0.025$ without significant losses in ground state fidelity, while substantially cutting down the circuit depth.

The 2×2 lattice with periodic boundary conditions has a large number of matrix elements at energy truncations higher than T_1 , as reflected in Fig. 1: there are $\sim 10^5$ matrix elements for the $B = 5.67$ and $B = 6.0$ truncations. This translates to gate counts of order a million for the EM and EMEM circuits for this lattice. Even though the gate counts for $B = 5.67$ and $B = 6.0$ are similar, performing a VQE for $B = 6.0$ proves to be computationally harder because encoding a $B = 6.0$ lattice requires 28 qubits (3 qubits per link for the irreps $\{1, 3, \bar{3}, 8, 6, \bar{6}\}$ and 4 site qubits) compared to 20 qubits for $B = 5.67$ (2 qubits per link for the irreps $\{1, 3, \bar{3}, 8\}$ and 4 site qubits). It should also be possible to substantially reduce the gate cost associated with the large number of magnetic transitions; the simplest method is to cut out transitions with small matrix elements.

The 5×1 lattice with the $B = 4.0$ truncation has a large qubit cost: 30 qubits are needed to encode the 15 links with periodic boundary conditions. However, the number of matrix elements in N -plaquette chains with a low energy truncation is significantly lower than the two dimensional lattice because of the simplicity of the site singlets. For $B = 4.0$ each site in the N plaquette chain has a maximum multiplicity of 1. This, combined with a straightforward control scheme for the plaquette chain lattices, leads to Trotter step gate counts $\sim 10^4$ for the 5 plaquette chain, 100 times smaller than the 2×2 case. The N -plaquette chain therefore seems to be the ideal candidate to test the ground state preparation methods developed in earlier sections for larger lattice sizes. However we also note that $N \times 1$ lattices are likewise more suitable for classical tensor network methods.

Lattice	Qubits	Method	CX Gate Count
Cube ($B = 4.0$)	24	VQE-MTI	8,000
		VQE-EM	26,000
		Adiabatic	8×10^6
		Hyb-Ad	6×10^5
2×2 ($B = 5.67$)	20	VQE-EM	1×10^6
		VQE-EMEM	2×10^6
2×2 ($B = 6.0$)	28	VQE-EM	1.8×10^6
		VQE-EMEM	3.6×10^6
5×1 ($B = 4.0$)	30	VQE-EM	18,000
		VQE-EMEM	36,000
		Hyb-Ad	7×10^5

Table 5: Quantum resource costs for different methods of state preparation.

4 Simulation code: `ymcirc`

We conclude by describing `ymcirc`, a Python code package for SU(3) quantum simulations which we make available with this work. `ymcirc` includes tools for automated construction of time-evolution and ground-state preparation circuits, as well as the interpretation of circuit measurement data. At the time of writing, the latest active development release may be accessed at <https://github.com/hepqis-uiuc/ymcirc>.³

The supplementary material for this paper consists of a Jupyter Notebook demonstrating the use of `ymcirc` to generate, simulate, and interpret lattice time-evolution circuits.

4.1 Available functionality

One of the primary goals of `ymcirc` is to automate to the greatest degree possible the complicated bit/qubit indexing which arises when constructing lattice simulation circuits

³Magnetic Hamiltonian matrix element data present in `ymcirc` were precomputed using the `pyclebsch` Python package, which we have also made available at <https://github.com/hepqis-uiuc/pyclebsch>.

or interpreting simulation results. This is achieved via separate classes which (1) perform encoding or decoding between physical link or plaquette irrep data and bit strings, (2) arrange `qiskit`'s quantum register classes into an logical lattice data structure which can be indexed via lattice coordinates, (3) arrange measurements⁴ of a circuit constructed with `ymcirc` into an analogous lattice data structure indexable by lattice coordinates, (4) functionality for computing electric energy eigenvalues, (5) type aliases which serve as aids to the user for constructing valid irrep weight and multiplicity data, and physical plaquette states, and (6) pre-defined irrep weights for **1**, **3**, **3̄**, **8**, **6**, and **6̄**.

Additional functionality in the development version of `ymcirc` available at time of writing includes:

- Circuit generation for first-order Trotterization of electric and magnetic time evolution for periodic lattices in $d = 3/2$ and $d = 2$, with step size and magnetic coupling parameterized per-Trotter step. There is also an option to expose each individual Givens rotation in a magnetic Trotter step as a tuneable parameter for VQE state prep.
- Irrep truncation magnetic Hamiltonian data for T_1 and T_2 in $d = 3/2$, and T_1 in $d = 2$.
- Magnetic Hamiltonian matrix element data computed from symmetrized CGCs.
- Primitive functions for generating individual Givens rotation circuits.
- Classes for defining the geometry of lattices, as well as traversing data on a lattice in a consistent order.
- Circuit-depth reduction methods from [15] such as control pruning, control fusion, and gray ordering of gates, as well as an optional ‘v-chain’ construction of *MCX* gates via ancilla qubits [61, 62]).

4.2 Development roadmap

At present, the circuit generation capabilities of `ymcirc` are limited to $d = 3/2$ and $d = 2$ for a small selection of irrep truncation schemes. This informs what is the most immediate future development goal: to extend circuit construction to higher dimensionality, and include a greater variety of irrep truncation options (such as the B -parameter scheme used in this paper).

Other items in near-to-intermediate term development pipeline include:

- F -orderings (needed for $d \geq 3$ circuit generation).
- Open/mixed boundary conditions.
- Rectangular lattices for $d \geq 2$.

⁴Both decoded physical irrep data or the underlying bit string measurement data are included.

- Classes for specifying local circuit measurements via lattice coordinates.
- Classes for computing observables from local measurement results.
- (Longer-term) Incorporating matter degrees of freedom.

5 Conclusion and Future Directions

We conclude by summarizing the technical and numerical results reported in this work toward the quantum simulation of $SU(3)$ LGT, and some directions for future work. On the technical front, we utilize and extend the reduced electric basis introduced in [15] by introducing a more fine-grained irrep truncation scheme (the “ B ” truncations), and by reducing the number of \square matrix elements through the permutation group properties of the $SU(3)$ irreps. We also introduce variational ansätze, based on strong coupling perturbation theory, for use in ground state preparation at $g \sim 1$. We benchmark this framework on plaquette chains, the 2×2 -plaquette lattice, and the 6-plaquette cube with open boundary conditions, performing noiseless simulations on systems of up to 30 qubits. Variational methods, adiabatic state preparation, and hybrid variational-adiabatic methods are found to achieve fidelities $1 - F$ better than a few percent at $g = 1$. Finally, alongside this work, we introduce a public-use python suite, `ymcirc`, to efficiently generate and run lattice evolution circuits in the reduced electric basis.

There are several directions for extension. To apply variational methods to larger systems, we need a stitching procedure, as in [44], and/or an efficient and systematic way to measure the energy expectation value of the system (or stitchable subsystems), $\text{Tr}(H\rho(\theta))$, on a quantum device, where ρ is an output VQE state at each iteration. There are various methods to measure the expectation value, including random basis sampling and quantum state tomography [63, 64], but generally they incur a high cost in state preparation circuits. It remains to be seen whether such methods can be tailored in an efficient way for LGT simulations. For larger systems it may also be useful to work at higher orders in perturbation theory when formulating variational ansatz states; this extension should be straightforward.

It may also be useful to examine hybrid variational-adiabatic approaches to ground state preparation more deeply [65, 66]. It would be useful, for example, to have a procedure to estimate the optimal switching point between variational and adiabatic methods.

Finally, a substantial challenge in performing interesting simulations on real hardware, or more accurate simulations on future hardware, is the large gate depth associated primarily with the plaquette-local magnetic Hamiltonian. Improving the quantum algorithms used to encode plaquette operators would have a tangible impact on the simulation approach used here.

Acknowledgments

We acknowledge the support of the U.S. Department of Energy, Office of Science, Office of High Energy Physics Quantum Information Science Enabled Discovery (QuantISED) program. This work used the Delta system at the National Center for Supercomputing Applications through allocation PHY230137 from the Advanced Cyberinfrastructure Coordination Ecosystem: Services & Support (ACCESS) program, which is supported by National Science Foundation grants #2138259, #2138286, #2138307, #2137603, and #2138296.

References

- [1] C. W. Bauer, Z. Davoudi, A. B. Balantekin, T. Bhattacharya, M. Carena, W. A. de Jong, P. Draper, A. El-Khadra, N. Gemelke, M. Hanada, D. Kharzeev, H. Lamm, Y.-Y. Li, J. Liu, M. Lukin, Y. Meurice, C. Monroe, B. Nachman, G. Pagano, J. Preskill, E. Rinaldi, A. Roggero, D. I. Santiago, M. J. Savage, I. Siddiqi, G. Siopsis, D. Van Zanten, N. Wiebe, Y. Yamauchi, K. Yeter-Aydeniz, and S. Zorzetti, “Quantum simulation for high-energy physics,” *PRX Quantum* **4** (May, 2023) 027001. <https://link.aps.org/doi/10.1103/PRXQuantum.4.027001>.
- [2] C. W. Bauer, Z. Davoudi, N. Klco, and M. J. Savage, “Quantum simulation of fundamental particles and forces,” *Nature Reviews Physics* **5** no. 7, (June, 2023) 420–432. <http://dx.doi.org/10.1038/s42254-023-00599-8>.
- [3] A. Di Meglio, K. Jansen, I. Tavernelli, C. Alexandrou, S. Arunachalam, C. W. Bauer, K. Borras, S. Carrazza, A. Crippa, V. Croft, R. de Putter, A. Delgado, V. Dunjko, D. J. Egger, E. Fernández-Combarro, E. Fuchs, L. Funcke, D. González-Cuadra, M. Grossi, J. C. Halimeh, Z. Holmes, S. Kühn, D. Lacroix, R. Lewis, D. Lucchesi, M. L. Martinez, F. Meloni, A. Mezzacapo, S. Montangero, L. Nagano, V. R. Pascuzzi, V. Radescu, E. R. Ortega, A. Roggero, J. Schuhmacher, J. Seixas, P. Silvi, P. Spentzouris, F. Tacchino, K. Temme, K. Terashi, J. Tura, C. Tüysüz, S. Vallecorsa, U.-J. Wiese, S. Yoo, and J. Zhang, “Quantum computing for high-energy physics: State of the art and challenges,” *PRX Quantum* **5** (Aug, 2024) 037001. <https://link.aps.org/doi/10.1103/PRXQuantum.5.037001>.
- [4] J. C. Halimeh, N. Mueller, J. Knolle, Z. Papić, and Z. Davoudi, “Quantum simulation of out-of-equilibrium dynamics in gauge theories,” 2025. <https://arxiv.org/abs/2509.03586>.
- [5] **NuQS Collaboration** Collaboration, H. Lamm, S. Lawrence, and Y. Yamauchi, “Parton physics on a quantum computer,” *Phys. Rev. Res.* **2** (Mar, 2020) 013272. <https://link.aps.org/doi/10.1103/PhysRevResearch.2.013272>.
- [6] J.-W. Chen, Y.-T. Chen, and G. Meher, “Parton distributions on a quantum computer,” 2025. <https://arxiv.org/abs/2506.16829>.

- [7] R. C. Farrell, M. Illa, and M. J. Savage, “Steps toward quantum simulations of hadronization and energy loss in dense matter,” *Phys. Rev. C* **111** (Jan, 2025) 015202. <https://link.aps.org/doi/10.1103/PhysRevC.111.015202>.
- [8] J. Barata and E. Rico, “Real-time simulation of jet energy loss and entropy production in high-energy scattering with matter,” 2025. <https://arxiv.org/abs/2502.17558>.
- [9] Z. Davoudi, N. Mueller, and C. Powers, “Towards quantum computing phase diagrams of gauge theories with thermal pure quantum states,” *Phys. Rev. Lett.* **131** (Aug, 2023) 081901. <https://link.aps.org/doi/10.1103/PhysRevLett.131.081901>.
- [10] A. T. Than, Y. Y. Atas, A. Chakraborty, J. Zhang, M. T. Diaz, K. Wen, X. Liu, R. Lewis, A. M. Green, C. A. Muschik, and N. M. Linke, “The phase diagram of quantum chromodynamics in one dimension on a quantum computer,” 2024. <https://arxiv.org/abs/2501.00579>.
- [11] J. Kogut and L. Susskind, “Hamiltonian formulation of wilson’s lattice gauge theories,” *Phys. Rev. D* **11** (Jan, 1975) 395–408. <https://link.aps.org/doi/10.1103/PhysRevD.11.395>.
- [12] E. Zohar and M. Burrello, “Formulation of lattice gauge theories for quantum simulations,” *Phys. Rev. D* **91** (Mar, 2015) 054506. <https://link.aps.org/doi/10.1103/PhysRevD.91.054506>.
- [13] T. Byrnes and Y. Yamamoto, “Simulating lattice gauge theories on a quantum computer,” *Phys. Rev. A* **73** (Feb, 2006) 022328. <https://link.aps.org/doi/10.1103/PhysRevA.73.022328>.
- [14] A. Ciavarella, N. Klco, and M. J. Savage, “Trailhead for quantum simulation of su(3) yang-mills lattice gauge theory in the local multiplet basis,” *Phys. Rev. D* **103** (May, 2021) 094501. <https://link.aps.org/doi/10.1103/PhysRevD.103.094501>.
- [15] P. Balaji, C. Conefrey-Shinozaki, P. Draper, J. K. Elhaderi, D. Gupta, L. Hidalgo, A. Lytle, and E. Rinaldi, “Quantum circuits for su(3) lattice gauge theory,” 2025. <https://arxiv.org/abs/2503.08866>.
- [16] A. N. Ciavarella and C. W. Bauer, “Quantum simulation of su(3) lattice yang-mills theory at leading order in large- N_c expansion,” *Phys. Rev. Lett.* **133** (Sep, 2024) 111901. <https://link.aps.org/doi/10.1103/PhysRevLett.133.111901>.
- [17] A. N. Ciavarella, I. M. Burbano, and C. W. Bauer, “Efficient truncations of su(n_c) lattice gauge theory for quantum simulation,” 2025. <https://arxiv.org/abs/2503.11888>.
- [18] I. Raychowdhury and J. R. Stryker, “Loop, string, and hadron dynamics in su(2) hamiltonian lattice gauge theories,” *Phys. Rev. D* **101** (Jun, 2020) 114502. <https://link.aps.org/doi/10.1103/PhysRevD.101.114502>.

[19] S. V. Kadam, I. Raychowdhury, and J. R. Stryker, “Loop-string-hadron formulation of an $su(3)$ gauge theory with dynamical quarks,” *Phys. Rev. D* **107** (May, 2023) 094513. <https://link.aps.org/doi/10.1103/PhysRevD.107.094513>.

[20] S. V. Kadam, A. Naskar, I. Raychowdhury, and J. R. Stryker, “Loop-string-hadron approach to $su(3)$ lattice yang-mills theory: Hilbert space of a trivalent vertex,” *Phys. Rev. D* **111** (Apr, 2025) 074516. <https://link.aps.org/doi/10.1103/PhysRevD.111.074516>.

[21] J. Jiang, N. Klco, and O. D. Matteo, “Non-abelian dynamics on a cube: improving quantum compilation through qudit-based simulations,” 2025. <https://arxiv.org/abs/2506.10945>.

[22] A. H. Z. Kavaki and R. Lewis, “From square plaquettes to triamond lattices for $su(2)$ gauge theory,” *Communications Physics* **7** no. 1, (June, 2024) 208. <http://dx.doi.org/10.1038/s42005-024-01697-4>.

[23] A. H. Z. Kavaki and R. Lewis, “False vacuum decay in triamond lattice gauge theory,” *Phys. Rev. D* **112** (Jul, 2025) 014502. <https://link.aps.org/doi/10.1103/1km8-3tc3>.

[24] A. Kan, L. Funcke, S. Kühn, L. Dellantonio, J. Zhang, J. F. Haase, C. A. Muschik, and K. Jansen, “Investigating a $(3+1)D$ topological θ -term in the hamiltonian formulation of lattice gauge theories for quantum and classical simulations,” *Phys. Rev. D* **104** (Aug, 2021) 034504. <https://link.aps.org/doi/10.1103/PhysRevD.104.034504>.

[25] A. Kan and Y. Nam, “Lattice quantum chromodynamics and electrodynamics on a universal quantum computer,” 2022. <https://arxiv.org/abs/2107.12769>.

[26] **NuQS Collaboration** Collaboration, H. Lamm, S. Lawrence, and Y. Yamauchi, “General methods for digital quantum simulation of gauge theories,” *Phys. Rev. D* **100** (Aug, 2019) 034518. <https://link.aps.org/doi/10.1103/PhysRevD.100.034518>.

[27] M. Carena, H. Lamm, Y.-Y. Li, and W. Liu, “Improved hamiltonians for quantum simulations of gauge theories,” *Phys. Rev. Lett.* **129** (Jul, 2022) 051601. <https://link.aps.org/doi/10.1103/PhysRevLett.129.051601>.

[28] E. J. Gustafson, H. Lamm, and F. Lovelace, “Primitive quantum gates for an $su(2)$ discrete subgroup: Binary octahedral,” *Phys. Rev. D* **109** (Mar, 2024) 054503. <https://link.aps.org/doi/10.1103/PhysRevD.109.054503>.

[29] E. J. Gustafson, Y. Ji, H. Lamm, E. M. Murairi, S. O. Perez, and S. Zhu, “Primitive quantum gates for an $su(3)$ discrete subgroup: $\Sigma(36 \times 3)$,” *Phys. Rev. D* **110** (Aug, 2024) 034515. <https://link.aps.org/doi/10.1103/PhysRevD.110.034515>.

[30] J. F. Haase, L. Dellantonio, A. Celi, D. Paulson, A. Kan, K. Jansen, and C. A. Muschik, “A resource efficient approach for quantum and classical simulations of gauge theories in particle physics,” *Quantum* **5** (Feb., 2021) 393. <https://doi.org/10.22331/q-2021-02-04-393>.

[31] I. D'Andrea, C. W. Bauer, D. M. Grabowska, and M. Freytsis, “New basis for hamiltonian su(2) simulations,” *Phys. Rev. D* **109** (Apr, 2024) 074501. <https://link.aps.org/doi/10.1103/PhysRevD.109.074501>.

[32] D. M. Grabowska, C. F. Kane, and C. W. Bauer, “Fully gauge-fixed su(2) hamiltonian for quantum simulations,” *Phys. Rev. D* **111** (Jun, 2025) 114516. <https://link.aps.org/doi/10.1103/PhysRevD.111.114516>.

[33] I. M. Burbano and C. W. Bauer, “Gauge loop-string-hadron formulation on general graphs and applications to fully gauge fixed hamiltonian lattice gauge theory,” 2024. <https://arxiv.org/abs/2409.13812>.

[34] P. Fontana, M. Miranda-Riaza, and A. Celi, “Efficient finite-resource formulation of non-abelian lattice gauge theories beyond one dimension,” *Phys. Rev. X* **15** (Sep, 2025) 031065. <https://link.aps.org/doi/10.1103/k9p6-c649>.

[35] S. P. Jordan, K. S. M. Lee, and J. Preskill, “Quantum algorithms for quantum field theories,” *Science* **336** no. 6085, (June, 2012) 1130–1133. <http://dx.doi.org/10.1126/science.1217069>.

[36] A. Peruzzo, J. McClean, P. Shadbolt, M.-H. Yung, X.-Q. Zhou, P. J. Love, A. Aspuru-Guzik, and J. L. O’Brien, “A variational eigenvalue solver on a photonic quantum processor,” *Nature Communications* **5** no. 1, (July, 2014) 4213. <http://dx.doi.org/10.1038/ncomms5213>.

[37] J. Tilly, H. Chen, S. Cao, D. Picozzi, K. Setia, Y. Li, E. Grant, L. Wossnig, I. Rungger, G. H. Booth, and J. Tennyson, “The variational quantum eigensolver: A review of methods and best practices,” *Physics Reports* **986** (Nov., 2022) 1–128. <http://dx.doi.org/10.1016/j.physrep.2022.08.003>.

[38] Y. Y. Atas, J. Zhang, R. Lewis, A. Jahanpour, J. F. Haase, and C. A. Muschik, “Su(2) hadrons on a quantum computer via a variational approach,” *Nature Communications* **12** no. 1, (Nov., 2021) 6499. <http://dx.doi.org/10.1038/s41467-021-26825-4>.

[39] R. C. Farrell, I. A. Chernyshev, S. J. M. Powell, N. A. Zemlevskiy, M. Illa, and M. J. Savage, “Preparations for quantum simulations of quantum chromodynamics in 1 + 1 dimensions. i. axial gauge,” *Phys. Rev. D* **107** (Mar, 2023) 054512. <https://link.aps.org/doi/10.1103/PhysRevD.107.054512>.

[40] J. Zhang, R. Ferguson, S. Kühn, J. F. Haase, C. Wilson, K. Jansen, and C. A. Muschik, “Simulating gauge theories with variational quantum eigensolvers in superconducting microwave cavities,” *Quantum* **7** (Oct., 2023) 1148. <https://doi.org/10.22331/q-2023-10-23-1148>.

[41] S. Schuster, S. Kühn, L. Funcke, T. Hartung, M.-O. Pleinert, J. von Zanthier, and K. Jansen, “Studying the phase diagram of the three-flavor schwinger model in the presence of a chemical potential with measurement- and gate-based quantum computing,” *Phys. Rev. D* **109** (Jun, 2024) 114508. <https://link.aps.org/doi/10.1103/PhysRevD.109.114508>.

[42] Z. Davoudi, C.-C. Hsieh, and S. V. Kadam, “Scattering wave packets of hadrons in gauge theories: Preparation on a quantum computer,” *Quantum* **8** (Nov., 2024) 1520. <https://doi.org/10.22331/q-2024-11-11-1520>.

[43] A. Crippa, K. Jansen, and E. Rinaldi, “Analysis of the confinement string in (2 + 1)-dimensional quantum electrodynamics with a trapped-ion quantum computer,” 2024. <https://arxiv.org/abs/2411.05628>.

[44] A. N. Ciavarella and I. A. Chernyshev, “Preparation of the su(3) lattice yang-mills vacuum with variational quantum methods,” *Phys. Rev. D* **105** (Apr, 2022) 074504. <https://link.aps.org/doi/10.1103/PhysRevD.105.074504>.

[45] H. R. Grimsley, S. E. Economou, E. Barnes, and N. J. Mayhall, “An adaptive variational algorithm for exact molecular simulations on a quantum computer,” *Nature Commun.* **10** (2019) 3007, [arXiv:1812.11173 \[quant-ph\]](https://arxiv.org/abs/1812.11173).

[46] R. C. Farrell, N. A. Zemlevskiy, M. Illa, and J. Preskill, “Digital quantum simulations of scattering in quantum field theories using w states,” 2025. <https://arxiv.org/abs/2505.03111>.

[47] R. C. Farrell, M. Illa, A. N. Ciavarella, and M. J. Savage, “Scalable Circuits for Preparing Ground States on Digital Quantum Computers: The Schwinger Model Vacuum on 100 Qubits,” *PRX Quantum* **5** no. 2, (2024) 020315, [arXiv:2308.04481 \[quant-ph\]](https://arxiv.org/abs/2308.04481).

[48] R. C. Farrell, M. Illa, A. N. Ciavarella, and M. J. Savage, “Quantum simulations of hadron dynamics in the schwinger model using 112 qubits,” *Phys. Rev. D* **109** (Jun, 2024) 114510. <https://link.aps.org/doi/10.1103/PhysRevD.109.114510>.

[49] N. A. Zemlevskiy, “Scalable quantum simulations of scattering in scalar field theory on 120 qubits,” *Phys. Rev. D* **112** (Aug, 2025) 034502. <https://link.aps.org/doi/10.1103/qr72-51v1>.

[50] I. A. Chernyshev, R. C. Farrell, M. Illa, M. J. Savage, A. Maksymov, F. Tripier, M. A. Lopez-Ruiz, A. Arrasmith, Y. de Sereville, A. Brodutch, C. Girotto, A. Kaushik, and M. Roetteler, “Pathfinding quantum simulations of neutrinoless double- β decay,” 2025. <https://arxiv.org/abs/2506.05757>.

[51] E. Gustafson, K. Sherbert, A. Florio, K. Shirali, Y. Chen, H. Lamm, S. Valgushev, A. Weichselbaum, S. E. Economou, R. D. Pisarski, and N. M. Tubman, “Surrogate-constructed scalable-circuits adaptive variational quantum eigensolver in the schwinger model,” *Phys. Rev. Appl.* **23** (Jun, 2025) 064002. <https://link.aps.org/doi/10.1103/PhysRevApplied.23.064002>.

[52] M. C. Bañuls, K. Cichy, J. I. Cirac, K. Jansen, and S. Kühn, “Efficient basis formulation for 1+1 dimensional SU(2) lattice gauge theory: Spectral calculations with matrix product states,” *Phys. Rev. X* **7** no. 4, (2017) 041046, [arXiv:1707.06434 \[hep-lat\]](https://arxiv.org/abs/1707.06434).

[53] N. Klco, J. R. Stryker, and M. J. Savage, “SU(2) non-Abelian gauge field theory in one dimension on digital quantum computers,” *Phys. Rev. D* **101** no. 7, (2020) 074512, [arXiv:1908.06935 \[quant-ph\]](https://arxiv.org/abs/1908.06935).

[54] A. Alex, M. Kalus, A. Huckleberry, and J. von Delft, “A numerical algorithm for the explicit calculation of $SU(N)$ and $SL(N, \mathbb{C})$ Clebsch–Gordan coefficients,” *Journal of Mathematical Physics* **52** no. 2, (02, 2011) 023507.
<https://doi.org/10.1063/1.3521562>.

[55] M. A. A. van Leeuwen, A. M. Cohen, and B. Lisser, “Lie, a package for lie group computations,” 1992.
<http://www-math.univ-poitiers.fr/~maavl/pdf/LiE-manual.pdf>.

[56] R. M. Fonseca, “Groupmath: A mathematica package for group theory calculations,” *Computer Physics Communications* **267** (Oct., 2021) 108085.
<http://dx.doi.org/10.1016/j.cpc.2021.108085>.

[57] J. Alcock-Zeilinger and H. Weigert, “Compact hermitian young projection operators,” *Journal of Mathematical Physics* **58** no. 5, (05, 2017) 051702.
<https://doi.org/10.1063/1.4983478>.

[58] J. J. Sakurai and J. Napolitano, *Modern Quantum Mechanics*. Cambridge University Press, 3 ed., 2020.

[59] W. Kirby, M. Motta, and A. Mezzacapo, “Exact and efficient Lanczos method on a quantum computer,” *Quantum* **7** (May, 2023) 1018.
<https://doi.org/10.22331/q-2023-05-23-1018>.

[60] A. C. Y. Li, A. Macridin, S. Mrenna, and P. Spentzouris, “Simulating scalar field theories on quantum computers with limited resources,” *Physical Review A* **107** no. 3, (Mar, 2023) . <http://dx.doi.org/10.1103/PhysRevA.107.032603>.

[61] S. Balaucă and A. Arusoaie, *Efficient Constructions for Simulating Multi Controlled Quantum Gates*, p. 179–194. Springer International Publishing, 2022.
http://dx.doi.org/10.1007/978-3-031-08760-8_16.

[62] A. Barenco, C. H. Bennett, R. Cleve, D. P. DiVincenzo, N. Margolus, P. Shor, T. Sleator, J. A. Smolin, and H. Weinfurter, “Elementary gates for quantum computation,” *Physical Review A* **52** no. 5, (Nov, 1995) 3457–3467.
<http://dx.doi.org/10.1103/PhysRevA.52.3457>.

[63] M. Kohda, R. Imai, K. Kanno, K. Mitarai, W. Mizukami, and Y. O. Nakagawa, “Quantum expectation-value estimation by computational basis sampling,” *Phys. Rev. Res.* **4** (Sep, 2022) 033173.
<https://link.aps.org/doi/10.1103/PhysRevResearch.4.033173>.

[64] M. Cramer, M. B. Plenio, S. T. Flammia, R. Somma, D. Gross, S. D. Bartlett, O. Landon-Cardinal, D. Poulin, and Y.-K. Liu, “Efficient quantum state tomography,” *Nature communications* **1** no. 1, (2010) 149.

- [65] M.-C. Chen, M. Gong, X. Xu, X. Yuan, J.-W. Wang, C. Wang, C. Ying, J. Lin, Y. Xu, Y. Wu, *et al.*, “Demonstration of adiabatic variational quantum computing with a superconducting quantum coprocessor,” *Physical Review Letters* **125** no. 18, (2020) 180501.
- [66] S. M. Harwood, D. Trenev, S. T. Stober, P. Barkoutsos, T. P. Gujarati, S. Mostame, and D. Greenberg, “Improving the variational quantum eigensolver using variational adiabatic quantum computing,” *ACM Transactions on Quantum Computing* **3** no. 1, (2022) 1–20.
- [67] H. Georgi, *Lie Algebras in Particle Physics: From Isospin to Unified Theories*. CRC Press, May, 2018. <http://dx.doi.org/10.1201/9780429499210>.
- [68] W. Fulton, *Representation theory: a first course*. Graduate texts in mathematics ; 129. Readings in mathematics. Springer-Verlag, New York, 1991.
- [69] A. N. Sengupta, *Representing Finite Groups*. Springer New York, 2012. <http://dx.doi.org/10.1007/978-1-4614-1231-1>.

A Exact Diagonalization

This appendix gives an overview of simple implementations of exact diagonalization (ED) and how the complexity scales for different lattices and truncations. For Hilbert spaces that are not too large, the Hamiltonian can be exactly diagonalized or exponentiated using common computational linear-algebra libraries. Furthermore the local nature of the electric basis means the matrix representation for the Hamiltonian is sparse and can thus benefit from more memory- and CPU/GPU-efficient algorithms. In this paper we use the `scipy.sparse` package for its versatility and ease-of-use. After picking a lattice dimension and truncation, a matrix representation for the action of the plaquette operator $\square + \square^\dagger$ is built directly from a table of precomputed master formula coefficients in a tensor-product basis of the vertex sites and links. Note that it is often more efficient to encode the state space using the minimal degrees of freedom necessary rather than a direct embedding of the qubitized Hamiltonian. For instance, with a T_1 truncation the dimension of the link space is three-dimensional so a “qutrit” representation is more efficient. The local plaquette operator matrix representation is then embedded in the Hamiltonian of the full Hilbert space with `scipy.sparse.kron` for each distinct plaquette of the system N_P . The electric Casimir operator E^2 is diagonal and formulaic in this basis and thus the matrix representation is simple to make. Once constructed, the total matrix can be diagonalized using `scipy.sparse.linalg.eigsh` to find the groundstate energy and eigenvector, or exponentiated using `.expm_multiply` to find the dynamical wavefunction $|\psi(t)\rangle = \exp(-iHt)|0\rangle$.

These `scipy.sparse` algorithms call matrix multiplication algorithms written in C and C++ which have complexity that scales $\mathcal{O}(n_{\text{nnz}} + n_{\text{row}})$ where n_{nnz} is the number of nonzero entries and n_{row} is the number of rows in the matrix representation. Because of the large number of non-gauge invariant states in the electric basis and the sparsity of the magnetic

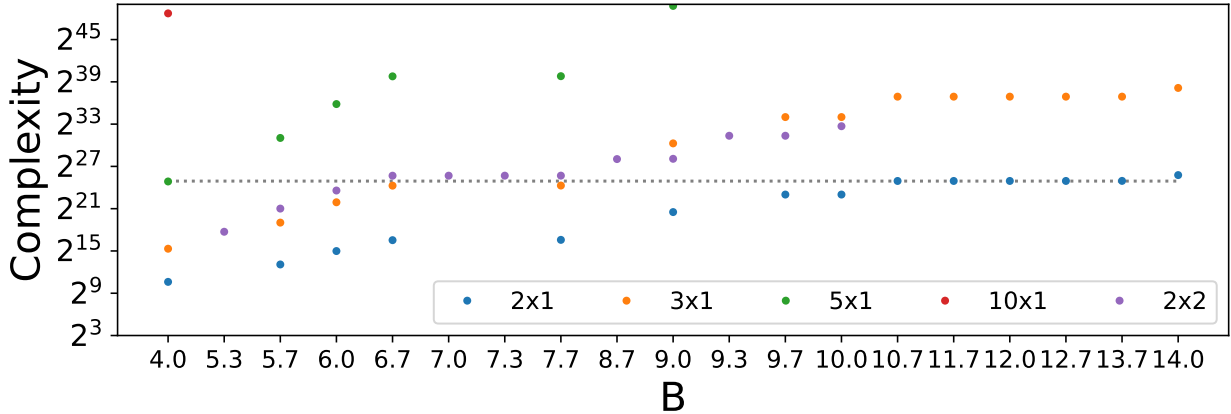


Figure S1: Classical exact diagonalization complexity $\mathcal{O}(\text{nnz} + n_{\text{row}})$ for different lattice dimensions e.g. $N \times 1$ and truncations at B cuts, assuming the reduced electric basis. The grey line denotes the upper limit of what we could implement on one node of Delta's 128 core CPU with 200GB of memory.

term, n_{row} is usually of comparable or greater order than n_{nnz} . For a given energy/irrep truncation given by B (see Section 2), $n_{\text{row}}(B)$ is $\ell^L \times v^V$ where ℓ is the number of irreps, L is the number of links, v is the maximum multiplicity at each vertex, and V is the number of vertices. $n_{\text{nnz}}(B)$ is $\mathcal{O}(P \times N_P \times F) + n_{\text{row}}$ where P is the number of nonzero entries to the local representation for \square , i.e. the number of \square matrix elements, N_P is the number of plaquettes, and F is the size of the lattice Hilbert space excluding the plaquette. This complexity value is plotted in Fig. S1 for different lattices and truncations. Depending on the specific algorithm chosen, the code implementation, the precision required, and the hardware used, resources like memory, CPU/GPU-usage, and wall time will vary. However it is clear that for large lattices with more than the bare minimum gauge-field truncation, the resource requirements quickly exceed the bounds of classical computation.

B Strong-Coupling Perturbation Theory Lowest Order Energy

For completeness we provide further details for the perturbation theory computation. The smallest gauge-invariant excitation of the lattice is the excitation of one plaquette $|p\rangle = (\square + \square^\dagger)|0\rangle$ at one site with unperturbed energy eigenvalue

$$E_p = \frac{8g^2}{3a^{d-2}}$$

coming from $\hat{H}_0 = \frac{1}{2}\hat{E}^2$. We showed in Section 3.1 that the normalized perturbed groundstate to lowest nontrivial order in g is

$$\begin{aligned} |0\rangle_N &= Z^{-\frac{1}{2}} (|0^{(0)}\rangle + \lambda |0^{(1)}\rangle) \\ &= \left(1 + \frac{9N_P a^{4d-12}}{32g^8}\right)^{-\frac{1}{2}} \left(|0^{(0)}\rangle + \frac{3a^{2d-6}}{8g^4} \sum_{\text{plaq}} \sum_{s=\square, \square^\dagger} |p, s\rangle\right) \end{aligned}$$

where N_P is the number of distinct plaquettes on the lattice. We can then compute the energy of this state (as a function of g)

$$\begin{aligned} E_0(g) &= Z^{-1} (\langle 0^{(0)} | + \lambda \langle 0^{(1)} |) (\hat{H}_0 + \lambda \hat{V}) (|0^{(0)}\rangle + \lambda |0^{(1)}\rangle) \\ &= Z^{-1} (\lambda^2 \langle 0^{(1)} | \hat{H}_0 | 0^{(1)} \rangle + 2\lambda^2 \langle 0^{(1)} | \hat{V} | 0^{(0)} \rangle + \lambda^3 \langle 0^{(1)} | \hat{V} | 0^{(1)} \rangle) \end{aligned}$$

Here we've already removed the $\langle 0^{(0)} | \hat{V} | 0^{(0)} \rangle$ and $\langle 0^{(0)} | \hat{H}_0 | 0^{(1)} \rangle$ terms due to orthogonality of the excited plaquette states. Looking at each term individually,

$$\lambda^2 \langle 0^{(1)} | \hat{H}_0 | 0^{(1)} \rangle = \frac{\lambda^2}{E_p^2} \sum_{p,s} \sum_{p',s'} \langle p, s | \hat{H}_0 | p', s' \rangle = \frac{3N_P a^{3d-10}}{4g^6}$$

$$2\lambda^2 \langle 0^{(1)} | \hat{V} | 0^{(0)} \rangle = -\frac{2\lambda^2}{E_p} \sum_{p,s} \langle p, s | \hat{V} | 0^{(0)} \rangle = -\frac{3N_P a^{3d-10}}{2g^6}$$

The last term relies on the fact that $1 = \langle 0^{(0)} | \hat{\square}^3 | 0^{(0)} \rangle = \langle \square^\dagger 0^{(0)} | \square^2 0^{(0)} \rangle$ which stems from the singlet in $3 \otimes 3 \otimes 3$. The $\langle 0^{(1)} | \hat{V} | 0^{(1)} \rangle$ term can then be interpreted as a sum over double excitations which match a single excitation, or triple excitations that match the ground state.

$$\lambda^3 \langle 0^{(1)} | \hat{V} | 0^{(1)} \rangle = \frac{\lambda^3}{E_p^2} \sum_{p,s} \sum_{p',s'} \langle p, s | \hat{V} | p', s' \rangle = \frac{2N_P \lambda^3}{E_p^2} = \frac{9N_P a^{5d-16}}{32g^{10}}$$

Thus all together

$$E_0(g) = -N_P \left(1 + \frac{9N_P a^{4d-12}}{32g^8}\right)^{-1} \left(\frac{3a^{3d-10}}{4g^6} + \frac{9a^{5d-16}}{32g^{10}}\right) \quad (32)$$

as written in Eqn 14.

C Permutation symmetries in direct-sum decompositions

We will briefly review how permutation symmetries emerge when considering direct-sum decompositions as well as the representation theory of the symmetric group S_n . Once these

preliminaries have been accomplished, we will be able to describe our procedure for computing CGCs in a basis that diagonalizes the permutation symmetries latent in the direct sum decomposition of $SU(N)$ tensor products.

We can understand how permutation symmetries emerge in computing direct-sum decompositions by considering two basic examples. First, there is the familiar example of the antisymmetric singlet and the fully-symmetric triplet appearing in the decomposition of two spin-1/2 particles. Second, consider the decomposition of the tensor product $3 \otimes 3$ in $SU(3)$ [67]. The product of two fundamental irreps, u^i and u^j , can be written as the sum of a totally symmetric two-index tensor and a totally antisymmetric one,

$$u^i u^j = \frac{1}{2} (u^i u^j + u^j u^i) + \frac{1}{2} \epsilon^{ijk} \epsilon_{klm} u^l u^m. \quad (33)$$

Symmetric tensors with two fundamental indices have six degrees of freedom, while antisymmetric tensors have three. The decomposition is:

$$3 \otimes 3 = 6^{(1,1)} \oplus \bar{3}^{(2)}, \quad (34)$$

where the superscript λ on each $SU(3)$ irrep labels the representation of the symmetric group which the $SU(3)$ irrep transforms under. In the current case, $\lambda = (1, 1)$ is the fully-symmetric representation of the permutation group S_2 , while $\lambda = (2)$ is the fully antisymmetric representation.

In general, irreps λ of the symmetric group S_n are labeled by partitions of n , which correspond to Young diagrams. The entries in a partition of n stipulate the number of boxes in each row of the Young diagram. For example,

$$(4, 2, 1) \leftrightarrow \begin{array}{c} \square \quad \square \quad \square \quad \square \\ \square \quad \square \\ \square \quad \square \\ \square \end{array} \quad (35)$$

labels an irreps of S_7 . The dimensionality of S_n irreps is given by the hook-length formula [68]. It is computed via the hook-length $h(i, j)$ of the (i, j) -th box in a Young diagram. $h(i, j)$ is the number of boxes in a ‘hook’ connecting all the boxes below the (i, j) -th one and all the boxes to the right of it. As an example, we label each box in the $(4, 2, 1)$ Young diagram with its hook length:

$$\begin{array}{c} \begin{array}{|c|c|c|c|} \hline 6 & 4 & 1 & 1 \\ \hline 3 & 1 & & \\ \hline 1 & & & \\ \hline \end{array} \end{array} \quad (36)$$

The hook-length formula gives the dimensionality of an irrep λ of S_n as

$$\dim \lambda = \frac{n!}{\prod_{(i,j)} h(i, j)}. \quad (37)$$

Continuing with our example of $\lambda = (4, 2, 1)$, we have that

$$\dim(4, 2, 1) = \frac{7!}{6 \cdot 4 \cdot 1 \cdot 1 \cdot 3 \cdot 1 \cdot 1} = 70. \quad (38)$$

By extension it is straightforward to see that the notation appearing in the direct-sum decomposition of $3 \otimes 3$ in Eqn. 34 indicates that the 6 and 3 transform in one-dimensional irreps of S_2 , as they must, since neither irrep is repeated. More generally a term R^λ appearing in a direct-sum decomposition denotes an $SU(N)$ irrep R which transforms in a representation λ of S_n . This notation can be understood as compactly denoting a product of the representations R and λ which collectively has dimension $\dim R \cdot \dim \lambda$.⁵

In the case of $3 \otimes 3$, we automatically obtained a direct-sum decomposition whose terms were also irreps of the symmetric group. When considering higher tensor powers of an $SU(N)$ irrep, $R^{\otimes n}$ with $n > 2$, this is no longer guaranteed. If we desire direct summands R'^λ which are also irreps of the S_n , we must explicitly perform some kind of procedure to obtain them.⁶

We achieve this via a slight modification of the algorithm given in [54] for numerically computing $SU(N)$ CGCs. The modification takes place at the point in that algorithm where a highest-weight state of an $SU(N)$ irrep has been obtained from a tensor product of $SU(N)$ irreps. At that point, we construct the set of *Hermitian Young projection operators* described in [57] which project onto irreps of the symmetric group, and apply them all to the highest weight state. This effectively splits the highest weight state into subspaces corresponding to irreps of S_n . From this point forward, our computation of CGCs continues to follow the procedure outlined in [54].

As an example of this procedure for ‘diagonalizing the permutation group symmetry,’ consider the direct-sum decomposition of $8 \otimes 8 \otimes 8$. Without diagonalizing the permutation group symmetry, we would write

$$8 \otimes 8 \otimes 8 = 64 \oplus 35'_2 \oplus 35_2 \oplus 27_6 \oplus 10'_4 \oplus 10_4 \oplus 8_8 \oplus 1_2, \quad (39)$$

where subscripts are present to denote nontrivial multiplicities of the irrep, and primes indicate distinct irreps which have the same dimensionality. If we instead use the modified procedure involving Hermitian Young projectors, we find that

$$\begin{aligned} 8 \otimes 8 \otimes 8 = & 64^{(3)} \oplus 35'^{(2,1)} \oplus 35^{(2,1)} \oplus 27^{(1,1,1)} \oplus 27_2^{(2,1)} \oplus 27^{(3)} \\ & \oplus 10'^{(1,1,1)} \oplus 10'^{(2,1)} \oplus 10'^{(3)} \oplus 10^{(1,1,1)} \oplus 10^{(2,1)} \oplus 10^{(3)} \\ & \oplus 8^{(1,1,1)} \oplus 8_3^{(2,1)} \oplus 8^{(3)} \oplus 1^{(1,1,1)} \oplus 1^{(3)}. \end{aligned} \quad (40)$$

We can focus on the subspaces of $8 \otimes 8 \otimes 8$ which transform in the 27 irrep to illustrate the difference between these results. The direct sum decomposition in Eqn 39 has six 27 irreps, which do not have clear transformation properties under the action of S_3 on $8 \times 8 \times 8$. In contrast, the direct sum decomposition in Eqn. 40 contains two 27 $SU(3)$ irreps which transform in one-dimensional irreps of S_3 and two pairs of 27 $SU(3)$ irreps which transform in two-dimensional representations of S_3 . In both cases, there is a 162-dimensional subspace containing six copies of the 27 $SU(3)$ irrep, but in the latter case, the CGCs affording the

⁵That the action of S_n and $SU(3)$ on tensor products of $SU(3)$ irreps commutes—and moreover that we can therefore determine a direct-sum decomposition in which each term consists of one $SU(3)$ irrep factor and one S_n irrep factor—is a manifestation of Schur-Weyl duality [69].

⁶In the context where R'^λ arises from computing the direct sum decomposition of $R^{\otimes n}$, it is referred to as a *symmetrized tensor product* or *plethysm* [55].

decomposition further block-diagonalize this subspace according the remaining permutation symmetry.